The Astrophysical Journal, 936:65 (24pp), 2022 September 1 https://doi.org/10.3847/1538-4357/ac83ac

Extragalactic Magnetism with SOFIA (SALSA Legacy Program). III. First Data Release and On-the-fly Polarization Mapping Characterization[*]

Enrique Lopez-Rodriguez[1], Melanie Clarke[2], Sachin Shenoy[2], William Vacca[2], Simon Coude[2], Ryan Arneson[2], Peter Ashton[2], Sarah Eftekharzadeh[2], Rainer Beck[3], John E. Beckman[4,5], Alejandro S. Borlaff[6], Susan E. Clark[1,7], Daniel A. Dale[8], Sergio Martin-Alvarez[9], Evangelia Ntormousi[10,11], William T. Reach[12], Julia Roman-Duval[13], Konstantinos Tassis[11,14], Doyal A. Harper[15], and Pamela M. Marcum[6]

[1] Kavli Institute for Particle Astrophysics & Cosmology (KIPAC), Stanford University, Stanford, CA 94305, USA; elopezrodriguez@stanford.edu
[2] SOFIA Science Center, NASA Ames Research Center, Moffett Field, CA 94035, USA
[3] Max-Planck-Institut für Radioastronomie, Auf dem Hügel 69, D-53121 Bonn, Germany
[4] Instituto de Astrofísica de Canarias, C/ Via Láctea s/n, E-38200 La Laguna, Tenerife, Spain
[5] Departamento de Astrofísica, Universidad de La Laguna, Avda. Astrofísico Fco. Sánchez s/n, E-38200 La Laguna, Tenerife, Spain
[6] NASA Ames Research Center, Moffett Field, CA 94035, USA
[7] Department of Physics, Stanford University, Stanford, CA 94305, USA
[8] Department of Physics & Astronomy, University of Wyoming, Laramie, WY 82071, USA
[9] Institute of Astronomy and Kavli Institute for Cosmology, University of Cambridge, Madingley Road, Cambridge CB3 0HA, UK
[10] Scuola Normale Superiore di Pisa, Piazza dei Cavalieri 7, I-56126 Pisa, Italy
[11] Institute of Astrophysics, Foundation for Research and Technology-Hellas, Vasilika Vouton, GR-70013 Heraklion, Greece
[12] Universities Space Research Association, NASA Ames Research Center, Moffett Field, CA 94035, USA
[13] Space Telescope Science Institute, 3700 San Martin Drive, Baltimore, MD 21218, USA
[14] Department of Physics & ITCP, University of Crete, GR-70013, Heraklion, Greece
[15] Department of Astronomy and Astrophysics, University of Chicago, Chicago, IL 60637, USA

Received 2022 April 24; revised 2022 July 9; accepted 2022 July 21; published 2022 August 31

Abstract

We describe the data processing of the Survey on extragALactic magnetiSm with SOFIA (SALSA Legacy Program). This first data release presents 33% (51.34 hr out of 155.7 hr, including overheads) of the total awarded time from 2020 January to 2021 December. Our observations were performed using the newly implemented on-the-fly mapping (OTFMAP) technique in the polarimetric mode. We present the pipeline steps to obtain homogeneously reduced high-level data products of polarimetric maps of galaxies for use in scientific analysis. Our approach has a general design and can be applied to sources smaller than the field of view of the HAWC+ array in any given band. We estimate that the OTFMAP polarimetric mode offers a reduction of observing overheads by a factor 2.34 and an improvement in sensitivity by a factor 1.80 when compared to the same on-source time polarimetric observations using the chopping and nodding mode. The OTFMAP is a significant optimization of the polarimetric mode of HAWC+, as it ultimately reduces the cost of operations of HAWC+/SOFIA by increasing the science collected per hour of observation up to an overall factor of 2.49. The OTFMAP polarimetric mode is the standard observing strategy of SALSA. The results and quantitative analysis of this first data release are presented in Papers IV and V of the series.

Unified Astronomy Thesaurus concepts: Polarimetry (1278); Extragalactic magnetic fields (507); Astronomy data reduction (1861); Far infrared astronomy (529); Seyfert galaxies (1447); Spiral galaxies (1560); Starburst galaxies (1570)

1. Introduction

Infrared (IR) observations from ground-based and suborbital telescopes are dominated by atmospheric thermal emission and telescope background emission. Revealing the astrophysical sources requires observing strategies that remove or minimize the competing contributions of these background emissions. The general approach is to observe the combined emission from the source and the background with a detector and then move the same detector to a part of the sky with only background emission. The offset between these two positions is performed on a timescale shorter than the background variation and the detector response. The subtraction of these two observations reveals the astrophysical source.

The chopping and nodding (C2N) strategy has been the most commonly used observing technique in the mid-IR (MIR; 8–30 μm) wavelength range (e.g., Burtscher et al. 2020, and references therein) and is sometimes used in the far-IR (FIR; 30–300 μm) wavelength range (e.g., Hildebrand et al. 2000). The secondary mirror alternates between an on-axis and an adjacent off-axis position on a fast cadence. The angular separations (i.e., chop throw) between on- and off-axis positions are usually within two to three fields of view (FOVs) of the array in a given band, yielding $\sim 5'' - 30''$ for MIR in 8 m class telescopes and up to $500''$ for FIR wavelengths. The cadence of < 1 s facilitates subtraction of fast sky variations. This telescope movement is known as chopping. Each pair of on-axis and off-axis images is subtracted to eliminate the background emission from the science image. However, as the secondary mirror is not aligned with the optical axis of the

---

[*] The SOFIA Legacy Program for Magnetic Fields in Galaxies (SALSA) provides a software repository at https://github.com/galmagfields/hawc and publicly available data at http://galmagfields.com/.

telescope while observing the nearby sky location, a residual background emission (also named radiative offset) is still present in the subtracted image. To minimize the radiative offset, the telescope is moved on its optical axis every $\leqslant 60$ s with the same, or different, amplitude and direction as the chopping configuration. A pair of subtracted chop-nod observations produces a positive image of the science object.

The C2N observing strategy has several disadvantages. First, although the residual offset is subtracted, final reduced images still have some level of background that generates emission patterns and/or residual levels of radiation that are not entirely removed. These residuals may arise from radiation of structures in the dome, sky variations, detector response variations, and/or dependencies of radiation offset as the telescope rotates. Note that for the C2N observations it is assumed that the spatial and temporal variations in the background emission from the on- and off-source positions are the same. However, the atmospheric background emission has spatial and temporal variations of $1/f^n$ (with $n > 1$), which implies that residuals after on- and off-axis position subtraction are inevitable. These residuals increase with both chop-throw and chop-nod frequency. Second, chop throws are usually $\leqslant 10''-500''$, which can complicate the background subtraction for objects with extended diffuse thermal emission (e.g., the Galactic center, star-forming regions, molecular clouds). Finally, this observing mode spends approximately half of the total observing time pointing to a nearby sky location away from the science object, which makes the observations inefficient with large overheads. As mentioned above, the final image is the subtracted on- and off-axis position with equal exposure times; thus, the final image has higher noise, by a factor $\sqrt{2}$, than the noise from a single pointing at the on-axis position.

The on-the-fly mapping (OTFMAP) strategy is an alternative observing mode in which the telescope on its optical axis scans the science object and surrounding areas. This technique is commonly used in the FIR and submillimeter wavelength ranges (e.g., Tegmark 1997; Hildebrand et al. 2000; Reichertz et al. 2001; Weferling et al. 2002; Waskett et al. 2007; Chapin et al. 2013). Single-dish radio telescopes also use this observing technique (Haslam 1974; Müller et al. 2017). This technique has recently gained attention in the MIR wavelength range (e.g., Ohsawa et al. 2018) owing to its prospects for the next generation of 30 m class telescopes. The telescope on its optical axis performs a scanning strategy (e.g., Kovács 2008a) described by a parametric curve and a mapping speed. The mapping speed is chosen such that the beam size (FWHM) of the instrument is oversampled at the sampling rate of the detector readout. For this configuration, (a) the sampling rate has to be at least twice the maximum frequency of the astrophysical and/or sky signal (i.e., spatial and temporal Nyquist sampling), and (b) the system noise must be comparable to or lower than the power spectrum of the sky at the desired spatial frequency to be recovered (e.g., Emerson & Graeve 1988).

The OTFMAP observing strategy presents advantages in terms of observing overheads, as at any given time the scan is integrating over a deeper image. In addition, the telescope can be moved to farther adjacent sky regions to reach "true" zero-level background emission. For bolometers, the signal is affected by both correlated and uncorrelated $1/f$-type noise, from the atmosphere, detectors, and readout electronics, which is characterized by having higher amplitudes at longer timescales. This behavior results in signal drifts that can affect all spatial structures in the final image. Most of the efforts of the OTFMAP strategy focus on the mapmaking algorithms and signal filtering to recover diffuse and extended emission from the astrophysical object. A mapmaking algorithm is required to reconstruct the sky image while subtracting the sky and detector variation responses (i.e., Kovács 2006; Waskett et al. 2007; Kovács 2008b; Patanchon et al. 2008; Cantalupo et al. 2010; Chapin et al. 2013; Roussel 2013). Note that the OTFMAP may also have structures in the background emission that increase with the structure size of the astrophysical object (when the size is larger than the FOV of the array) and inversely with scanning speed.

Chop-nod has been the standard observing strategy for the polarimetric mode of the High-resolution Airborne Wideband Camera-plus (HAWC+; Vaillancourt et al. 2007; Dowell et al. 2010; Harper et al. 2018) on board the 2.7 m Stratospheric Observatory For Infrared Astronomy (SOFIA). The OTFMAP observing mode had previously only been used for total intensity observations (Harper et al. 2018). Recent observations of galaxies Centaurus A (Lopez-Rodriguez 2021) and NGC 1097 (Lopez-Rodriguez et al. 2021) and the molecular clouds Taurus/L1495 (Li et al. 2022a) and OMC-3/4 (Li et al. 2022b) have successfully used the OTFMAP polarimetric mode with HAWC+. However, a full characterization of this new observing mode for HAWC+ has not been presented until now.

This manuscript describes the data reduction scheme of the OTFMAP polarimetric mode of HAWC+ for sources smaller than the FOV in any given band. In Section 2, we present the individual steps from raw data to high-level data products for use in scientific analysis. We present approaches for background subtraction, precipitable water vapor (PWV) correction, and flux and polarization calibration. In Section 3, we show a quantitative comparison between C2N and OTFMAP polarization modes and estimate the sensitivities for the OTFMAP observing mode. First results of this data release will be presented in Papers IV (Lopez-Rodriguez et al. 2022) and V (in preparation) of the series.

2. Observations and Data Reduction

2.1. Observations

New multiwavelength polarimetric observations of 10 galaxies were performed as part of the SOFIA Legacy Program[16] (ID: 08_0012; PI: E. Lopez-Rodriguez & S. A. Mao) using HAWC+ on the 2.7 m SOFIA telescope. This first data release presents 33% (51.34 hr out of 155.7 hr, including overheads) of the total awarded time from 2020 January to 2021 December. Table 1 shows the details of the new observations presented in this manuscript. In addition, we also include observations of Centaurus A (Lopez-Rodriguez 2021) at 89 μm and Circinus at 53, 89, and 214 μm from program ID 07_0032 (PI: E. Lopez-Rodriguez); M51 (Borlaff et al. 2021) at 154 μm under programs 70_0509 (Guaranteed Time Observations by the HAWC+ Team), 76_0003 (Discretionary Director Time), and 08_0260 (PI: Dowell, D.); and NGC 1097 (Lopez-Rodriguez et al. 2021) at 89 and 154 μm from program ID 07_0034 (PI: E. Lopez-Rodriguez). These additional observations comprised a total exposure time of 11.84 hr

---

[16] SOFIA Legacy Program on extragalactic magnetism can be found at http://galmagfields.com/.

Table 1
Summary of New OTFMAP Polarimetric Observations

Object (1)	Band (2)	Date (YYYYMMDD) (3)	Flight (4)	Altitude (kft) (5)	Scan Rate (arcsec s^{-1}) (6)	Scan Amplitude (EL × XEL; arcsec) (7)	Scan Duration (s) (8)	#Sets (bad) (9)	Obs. Time (s) (10)
Circinus[a]	A (53 μm)	20190716	F596	42	100	50 × 50	100	1(2)	400
								Total time	400 (0.11 hr)
	C (89 μm)	20190716	F596	41–42	100	70 × 70	100	2	800
						90 × 90	100	6	2400
								Total time	3200 (0.89 hr)
	E (214 μm)	20190716	F596	43	100	120 × 120	100, 60	2, 1	1040
								Total time	1040 (0.29 hr)
M82	A (53 μm)	20210505	F726	41–42	100	80 × 80	78, 60	1(2), 8(1)	2232
		20210513	F731	43	100	80 × 80	78	11	3432
								Total time	5664 (1.6 hr)
	C (89 μm)	20210518	F733	43	100	90 × 90	78	11	3432
		20210521	F736	42–43	100	90 × 90	78	8(3)	2496
								Total time	5928 (1.65 hr)
	D (153 μm)	20210520	F735	41–43	200	100 × 100	78	18	5616
		20210521	F736	42	200	100 × 100	78	5	1560
								Total time	7176 (1.99 hr)
	E (214 μm)	20210506	F727	39–40	200	180 × 180	78	3(3)	936
						210 × 210	78	7(1)	2184
		20210507	F728	39	200	210 × 210	78	0(1)	0
		20210511	F729	39	200	210 × 210	78	2	624
		20210513	F731	43	200	180 × 180	78	1(2)	312
								Total time	4056 (1.13 hr)
M83	D (154 μm)	20210512	F730	38–41	200	100 × 100	120	15 (1)	6720
		20210513	F731	41	200	100 × 100	120	8	3840
		20210520	F735	39–41	200	100 × 100	120, 60	16, 1	7920
		20210521	F736	39–42	200	100 × 100	120	10	4800
								Total time	23760 (6.60 hr)
NGC 253	C (89 μm)	20210901	F776	43	100	70 × 70	100	9	3600
								Total time	3600 (1.00 hr)
	D (154 μm)	20210915	F784	43	100	90 × 90	100	7(1)	3200
								Total time	3200 (0.89 hr)
NGC 1068	A (53 μm)	20210828	F774	43	100	60 × 60	120	3	1440
		20211103	F786	43	100	60 × 60	120, 45	6(1), 1	3060
								Total time	4500 (1.06 hr)
	C (89 μm)	20211207	F800	40–42	100	70 × 70	120, 60	11, 1	5520
		20211209	F802	42–43	100	70 × 70	120, 60	3(1), 1	1680
								Total time	7200 (2.00 hr)
NGC 1097[a]	D (154 μm)	20200128	F654	38	200	90 × 90	120	2	960
								Total time	960 (0.27 hr)
NGC 2146	A (53 μm)	20200125	F653	41–42	100, 60	30 × 30, 60 × 60	100	2, 1	1200
					100	60 × 60	60	2	480
		20200131	F657	40–42	100	30 × 30	100	3(2)	1200
							60	7	1680
		20210828	F774	43	100	30 × 30	100	0(12)	0
		20210831	F775	41	100	30 × 30	100	3	1200
								Total time	5760 (1.60 hr)
	C (89 μm)	20200130	F656	41	100	50 × 50	100	5(1)	2000
		20200131	F657	42	100	50 × 50	80	4(1)	1280
		20210914	F783	40–43	100	50 × 50	100	10(1)	4000
								Total time	7280 (2.02 hr)
	D (154 μm)	20200131	F657	42–43	100	70 × 70	80	2	640
						90 × 90	80, 60	4(1), 1	1200
		20210512	F730	42–43	200	100 × 100	100	12(3)	3600
		20210911	F782	41–42	200	100 × 100	100	4(3)	1600
		20210914	F783	40	200	100 × 100	100	4(1)	1600
								Total time	8640 (2.40 hr)
	E (214 μm)	20210512	F730	43	200	120 × 120	100	4(2)	1600
		20210519	F734	39	200	120 × 120	100	2(3)	800

Table 1
(Continued)

Object (1)	Band (2)	Date (YYYYMMDD) (3)	Flight (4)	Altitude (kft) (5)	Scan Rate (arcsec s^{-1}) (6)	Scan Amplitude (EL × XEL; arcsec) (7)	Scan Duration (s) (8)	#Sets (bad) (9)	Obs. Time (s) (10)
		20210831	F775	41–43	200	120 × 120	100	15	6000
								Total time	8400 (2.33 hr)
NGC 3627	D (154 μm)	20210511	F729	40-41	200	110 × 110	120	12(1)	5760
		20210514	F732	39–41	200	110 × 110	120	11(3)	5280
		20210519	F734	38	200	110 × 110	120	11(1)	5280
								Total time	16320 (4.53 hr)
NGC 4736	D (154 μm)	20211207	F800	43	200	110 × 100	102, 90	2, 12	5136
		20211208	F8001	43	200	170 × 170	102	7	2856
								Total time	7992 (2.22 hr)
NGC 4826	C (89 μm)	20210520	F735	43	200	110 × 110	100	4	1600
		20210521	F736	43	200	110 × 110	100	7	2800
								Total time	4400 (1.22 hr)
NGC 6946	D (154 μm)	20200909	F683	41–42	200	120 × 120	100	1	400
				42–43	200	180 × 180	80	17	5440
				43	200	220 × 220	80	1	360
		20200910	F684	43	200	120 × 120	80	1	320
						200 × 200	80, 60	2(4), 5(2)	1840
		20200911	F685	43	200	120 × 120	80	2	640
						180 × 180	100	14	5600
		20200922	F688	41–43	200	200 × 200	60, 90	12, 3	3960
		20200923	F689	42–43	200	180 × 180	80	10(1)	3200
		20200924	F690	41	200	200 × 200	80	13(1)	4160
								Total time	25920 (7.20 hr)
NGC 7331	D (154 μm)	20210511	F729	43	200	120 × 120	120	9	4320
		20210513	F731	43	200	120 × 120	120	7	3360
		20210514	F732	42–43	200	120 × 120	120, 90	12(1), 1	6120
		20210518	F733	43	200	120 × 120	120	2	960
		20210519	F734	40–43	200	120 × 120	120, 60	9, 1	4560
		20210903	F778	43	200	120 × 120	120, 60	3, 1	1680
		20210910	F781	43	200	120 × 120	120	2(4)	960
		20211103	F786	42	200	120 × 120	120	(4)	0
								Total time	21960 (6.10 hr)

Notes. Column (1): object name. Column (2): central wavelength of the band used for observations. Column (3): observation date (YYYYMMDD). Column (4): flight ID. Column (5): sea-level altitude during the observations. Column (6): speed of the scan. Column (7): amplitudes in elevation (EL) and cross-elevation (XEL) of the scan. Column (8): time per scan. Column (9): number of observation sets used (and rejected). Column (10): on-source observation time.

[a] Circinus observations from program ID 07_0032 (PI: E. Lopez-Rodriguez) and NGC 1097 observations from program ID 07_0034 (PI: E. Lopez-Rodriguez).

(including overheads) taken from 2017 to 2021. A total of 14 galaxies are presented in this data release.

All galaxies presented in this data release were homogeneously reduced using the steps presented below. For those galaxies already published, i.e., Centaurus A and NGC 1097, we reprocessed these data sets to produce data products within a homogeneous reduction scheme.

2.2. Data Reduction of the On-the-fly Map (OTFMAP) Polarimetric Mode

We performed observations using the OTFMAP polarimetric mode with HAWC+. This technique was an experimental observing mode used during the SOFIA Cycle 7 observations as part of engineering time (IDs: 71_0019 and 71_0023, PI: E. Lopez-Rodriguez) to optimize the polarimetric observations of HAWC+. This observing mode has been routinely used during SOFIA Cycles 8 and 9 for further characterization as part of the programmatic responsibilities of this SOFIA Legacy Program and offered in "shared-risk" mode for those proposals that desired to test this new observing mode. This technique was successfully applied to both galaxies (i.e., Centaurus A, Lopez-Rodriguez 2021; NGC 1097, Lopez-Rodriguez et al. 2021) and Galactic star-forming regions (the filamentary cloud Taurus/L1495, Li et al. 2022a; OMC-3/4, Li et al. 2022b). These early results were part of the SOFIA Cycle 7 and 8 observations. Here we describe the details of the OTFMAP polarimetric mode as the new observing strategy for HAWC+ on the study of magnetic fields in galaxies.

2.2.1. Processing Raw Data Using CRUSH

We reduced the raw data using the Comprehensive Reduction Utility for SHARC II v.2.50-1 (CRUSH; Kovács 2006, 2008b) and the HAWC_DRP_V2.7.0 pipeline developed by the data reduction pipeline group at the SOFIA Science Center.[17] SOFIA

---

[17] A full description of the most recent pipeline by the SOFIA Science Center can be found at https://www.sofia.usra.edu/data/data-analysis.

Table 2
HAWC+ Configuration

Band (1)	λ_c (μm) (2)	$\Delta\lambda$ (μm) (3)	Pixel Scale (arcsec) (4)	Beam Size (arcsec) (5)	Polarimetry FOV (arcmin) (6)
A	53	8.7	2.55	4.85	1.4 × 1.7
C	89	17	4.02	7.80	2.1 × 2.7
D	154	34	6.90	13.6	3.7 × 4.6
E	214	44	9.37	18.2	4.2 × 6.2

Note. Column (1): band name. Column (2): central wavelength of the band. Column (3): FWHM bandwidth. Column (4): pixel scale of the band. Column (5): FWHM. Column (6): FOV for polarimetric observations.

provided a version, HAWC_DRP_V3.0.0, that replaces CRUSH, written in JAVA, with a new version written in PYTHON. This new version[18] is a one-for-one drop-in replacement with all CRUSH's options included. The analysis presented here still holds for this new version.

HAWC+ polarimetric observations simultaneously measure two orthogonal components of linear polarization arranged in two arrays of 32 × 40 pixels each, labeled as reflective ($\mathcal{R}$) and transmissive ($\mathcal{T}$). Table 2 shows the characteristics of the HAWC+ bands, pixel scales, beam sizes (FWHM), and FOVs of the array for the polarimetric observations. For more information about HAWC+, we refer the reader to Harper et al. (2018).

The OTFMAP polarimetric mode performs observations in a sequence of four Lissajous scans, where each scan has a different half-wave plate (HWP) position angle (PA) in the following sequence: 5°, 50°, 27.°5, and 72.°5. A starting angle of 5° is chosen to avoid the reference position, 0°, of the HWP (Harper et al. 2018). This sequence is called a "set" hereafter (Figure 1, first row). In this HAWC+ observing mode, the telescope is driven to follow a parametric curve with a nonrepeating period whose shape is characterized by the relative phases and frequency of the motion. Each scan is characterized by its amplitude, rate, angles, and duration. Table 1 shows the Lissajous parameters for each galaxy (examples of Lissajous patterns are shown in Figures 10 and 16).

Each set was reduced using CRUSH, which estimates and removes the correlated atmospheric and instrumental signals, solves for the relative detector gains, and determines the noise weighting of the time streams in an iterative pipeline scheme. Each reduced scan produces two images associated with each array, $\mathcal{R}$ and $\mathcal{T}$. Both images are orthogonal components of linear polarization at a given HWP PA. At this stage, eight different images are computed (Figure 1, second row).

One of the limitations of the OTFMAP observing mode lies in the recovery of large-scale diffuse and faint emission from the astrophysical objects. This challenge is a result of the finite size of the array, variable atmosphere conditions, variable detector temperatures, scan rates, and the applied filters in the reduction steps used to recover extended emission. We applied several filters using CRUSH to recover large-scale emission structures of the galaxies while paying close attention to any change that may compromise the intrinsic polarization pattern of the astrophysical source. A total of 16 different pipeline schemes (e.g., FAINT, EXTENDED, BRIGHT, number of iterations, several filtering options) were performed per galaxy per band. For each of these pipeline schemes, the full data reduction steps were performed and statistical comparisons between the Stokes parameters IQU were computed. Specifically, flux conservation was compared between pipeline schemes. The morphologies between Stokes IQU per pipeline scheme and between Stokes I and PACS/Herschel observations at the closest wavelength were cross-correlated, and Anderson–Darling tests were conducted using the polarization fraction and angles between pipeline schemes. In addition, final products using these different schemes were compared to the galaxies with available C2N observations (M82, NGC 1068, and Circinus). We find that any additional options to the pipeline configuration described above introduce artificial polarization patterns to the galaxies. Some examples of the artificial polarization patterns include (a) constant PA of polarization across the FOV, (b) changes of the PA of polarization larger than 30° in regions of high signal-to-noise ratio in Stokes I ($\mathrm{S/N}_I \geqslant 500$), (c) additional extended structures in Stokes I that were not present in Herschel images, (d) flux calibration incompatible with Herschel images, and (e) differences in the PA of polarization of up to 50° when compared with the C2N observing mode. Thus, the standard pipeline using the nominal configuration for CRUSH provided by the SOFIA Science Center was used.

The angular extensions of all galaxies are within the polarimetry FOVs of the array in any given band (Table 2). For all observations, the final FOVs of the images have zero-level background, which enables a measure of the true sky background without contribution from the astrophysical object. Thus, the standard pipeline recovers the large-scale extended emission of the galaxies in our sample. In contrast, observations of molecular clouds or the Galactic center may have extended emission much larger than the polarimetry FOV in any given band. We point the reader to Taurus/L1495 observed with HAWC+ at 214 μm, where further pipeline steps were required to recover those large scales (Li et al. 2022a). For all the galaxies in our sample, observations with a sky rotation smaller than 3° were reduced within the same set, which increases the S/N per pixel to optimize the correlation between the astrophysical, sky, and instrumental signals. This approach optimizes the recovery of large scale and low surface brightness of the science object while keeping the rotation of the polarization angle vector within the intrinsic angular uncertainty of 3° of HAWC+ (Harper et al. 2018).

Table 1 shows several rejected sets for some galaxies, where 13% of the data were removed from the full sample. In general, these sets were removed owing to tracking issues during the observations, producing World Coordinate System (WCS) offsets in the time streams of the detector pixels that affect the mapmaking process. The worst-case scenario was found during the observations of NGC 2146 at 53 μm, flight F774. The object was found to have an offset from the position of the boresight of the array for each HWP PA during the full length of observations. Post-correction of the WCS as a function of the HWP PAs (a) did not fully correct the angular offsets and (b) produced a final product with polarization maps incompatible with the other flights. Given these issues, NGC 2146 observations in Band A during flight F774 were removed from the final data products.

---

[18] SOFIA data pipeline in PYTHON can be found at https://github.com/SOFIA-USRA/sofia_redux and https://www.sofia.usra.edu/data/data-pipelines.

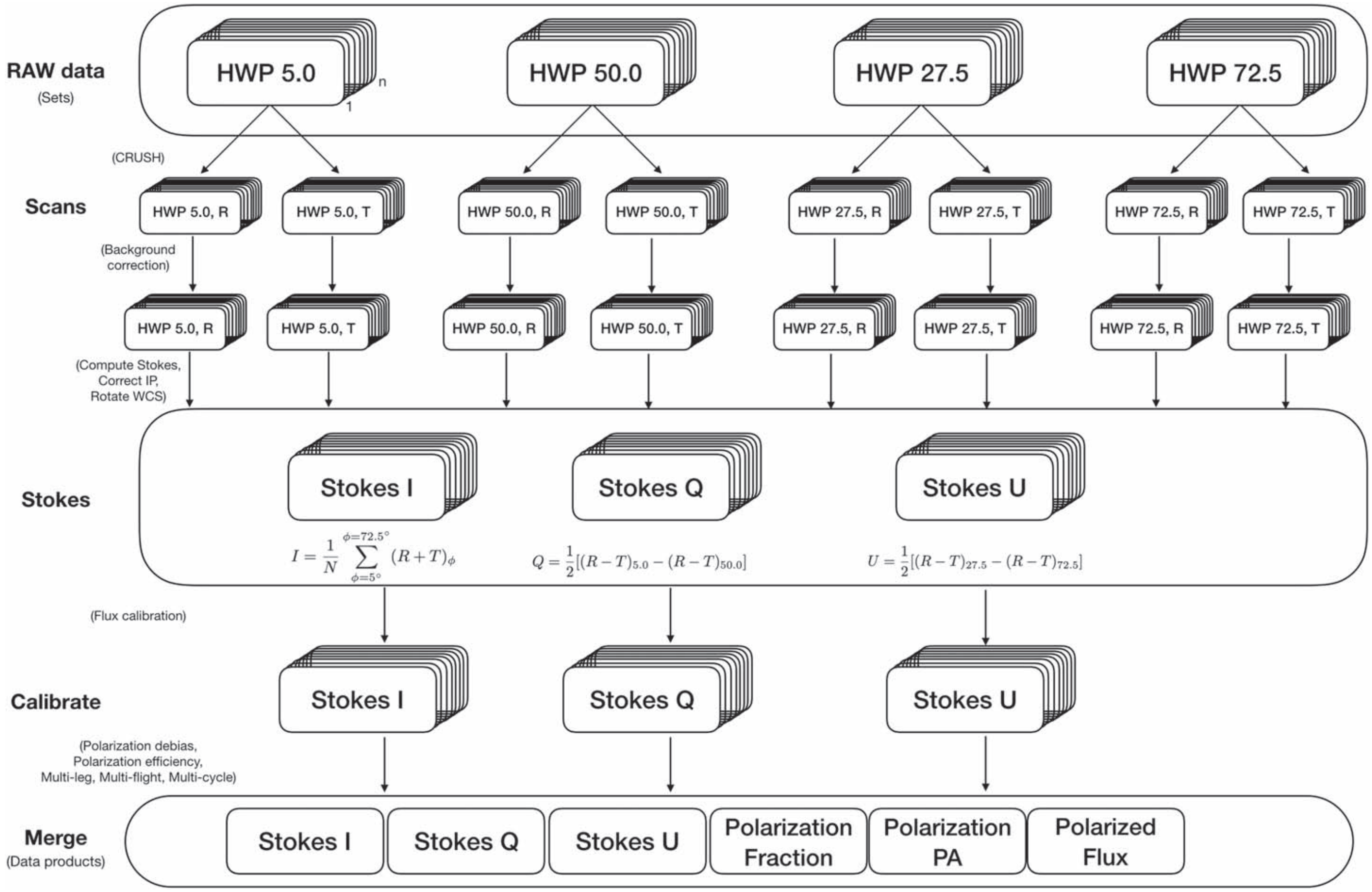

Figure 1. OTFMAP polarimetry data reduction flowchart. The raw data are combined in sets of four HWP PAs within a sky rotation tolerance of 3°. The sets are reduced using CRUSH, which generates a scan per $\mathcal{R}$ and $\mathcal{T}$ arrays and per HWP PA. Then, these scans are zero-level background corrected and combined, from which Stokes parameters are derived. After the Stokes parameters are corrected for IP, the scans are sky rotated and flux-calibrated. Finally, all Stokes parameters from different legs, flights, and/or cycles are merged to compute the final images, which contain Stokes *IQU*; polarization fraction, *P*; position angle, PA, of polarization; and polarized intensity, PI. The pipeline computes uncertainties and covariances, which are taken into account during all stages of the data reduction.

2.3. Zero-level Background Correction

HAWC+ measures the power of the emissive and variable atmosphere and the astrophysical object. The data reduction scheme described above may produce regions of negative flux in areas of extended and low surface brightness owing to the similar levels of noise and astrophysical signal. Thus, characterizing and estimating the zero-level background across the FOV of the observations of galaxies is imperative in mitigating the need to approximate and add the lost flux back to the full image later.

We have determined and corrected the zero-level background of our observations as follows. Since all galaxies are smaller than the HAWC+ FOV for a given band and they are isolated objects without large-scale extended thermal emission, the scan amplitudes (Table 1) were selected to have at least 1/3 of the final FOV with "true" zero-level background counts. In addition, the polarization skydips (Section 2.5) show that the sky is unpolarized. Thus, the sky background around the galaxies represents the "true" zero level, where flux and polarimetric calibration can be performed. Specifically, pixels with an S/N in total intensity $\geqslant 3$ were masked for each of the images per HWP PA and $\mathcal{R}$ and $\mathcal{T}$ arrays produced by CRUSH (Figure 1, second row). The masked background was fitted with a second-order surface and then added to the unmasked image, which ensures a positive background across the full FOV. The second-order surface has six free parameters, $f(x, y) = Ax^2 + By^2 + Cxy + Dx + Ey + F$, that were fit to the Nyquist-sampled images, generated in Section 2.2.1, using several hundred pixels. Using the Nyquist sampling or an individual pixel per beam did not affect the final fitting. We find that a second-order surface provides better results than a first-order (i.e., flat) surface. The background has similar curvature to the exposure maps, which have an exposure time that varies with the distance from the center of the image. This radial variation and the weighting computed by CRUSH per iteration produce the observed curvature in the background. As a test, this approach was also applied to unpolarized objects (i.e., planets), and the measured fluxes and instrumental polarization (IP) were found to be compatible with the C2N and skydip observing modes (Section 2.5). We estimated that the total flux from the second-order surface is $\leqslant 1\sigma$ of the pixel-to-pixel variation within each of individual scans, and the polarization associated with it is lower ($\leqslant 0.3\%$) than the IP ($\sim 1.6\%$–2.1%; Section 2.5) of HAWC+ in any given band. We speculate that this radial dependence may be due to a movement-dependent optical effect arising from slight deformations of the primary as the telescope is accelerated. The background at the map edges (highest acceleration) will always be systematically higher than the center of the map (lowest acceleration). We have corrected this effect by fitting the

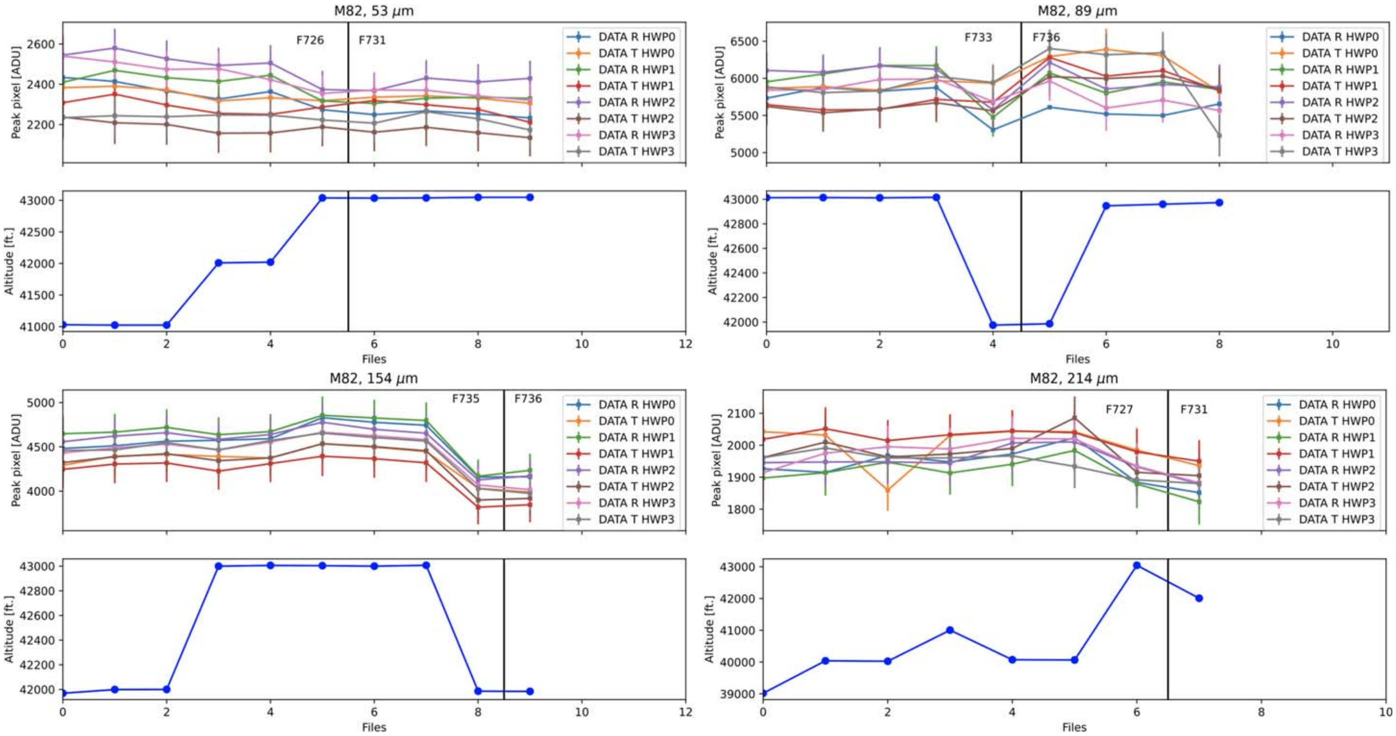

Figure 2. Example of flux variation as a function of time and aircraft altitude for M82 at all HAWC+ bands. Peak fluxes (first and third row) of the scans per HWP PA and $\mathcal{R}$ and $\mathcal{T}$ arrays at 53 μm (top left), 89 μm (top right), 154 μm (bottom left), and 214 μm (bottom right) of M82. The aircraft altitude (second and fourth rows) at the time of data acquisition is shown. The vertical lines show the boundaries between different flights.

background, but further characterization on the telescope acceleration is required for large maps (those maps larger than the FOV of the array).

A similar method was used in Taurus/L1495 by Li et al. (2022a), where a simpler approach to estimating the background in a C2N observation was performed. For these observations, an adjacent region equal to the FOV of the HAWC+ array close to the molecular cloud was identified using Herschel images. Using the HAWC+ observations, the mean of the background was estimated and considered as the zero-level background. Finally, the mean was added to the full FOV of the observations. These authors found that this technique contributed ∼14% to the polarized flux in their science observations. Here we use a second-order surface to fit the masked image after the removal of the astrophysical object. This approach provides lower artificial polarized flux and an optimal correction of the background structure. At this stage, eight different images with positive background are computed (Figure 1, third row).

2.4. Precipitable Water Vapor Correction

The standard pipeline corrects for the PWV based on the altitude of the aircraft at the time of the observations. As real-time PWV data are not available, this correction is performed using a model developed by the SOFIA Science Center that provides flux calibrations within a maximum of 20% uncertainty. If PWV variability and/or bad weather conditions were present during observations, further correction may be required to minimize flux variations that can affect the final flux calibration and/or polarization measurements.

We examined the flux variations of the scans per HWP PA and array after background correction for all galaxies as a function of the altitude and weather conditions. All galaxies show observed flux variations $\leqslant 15\%$ at all bands independently of the altitude and weather conditions. Figure 2 shows an example of flux variations as a function of time and aircraft altitude for all HAWC+ bands for M82. This figure demonstrates that flux variations are negligible during climbing in the flight profile. In addition, the relative flux contributions from HWP PAs and arrays are mostly constant, although the relative mean flux of the full scan may vary within the maximum 20% flux uncertainty. This result implies that the intrinsic polarization of the source is conserved relative to the altitude and weather conditions within a set of four HWP PAs.

The only exceptions are M83 and NGC 6946. We found that these galaxies have strong flux variations during several days of observations that cannot be explained by altitude changes or instrumental performance. Figure 3 shows the measured flux variations for M83 at 154 μm. Flights F735 and F736 have flux variations that exceed the nominal 20% flux uncertainties provided by HAWC+. These flux variations are not directly related to changes in the aircraft altitude (Figure 3(a) vs. Figure 4, bottom). Instead, changes in the PWV during the data acquisition explain the flux variations. The expected PWV was obtained based on satellite data used by the SOFIA Science Center and available to the users by demand. Specifically, flight F731 has a constant mean flux across the 1.5 hr of observations, with also a constant PWV of ∼11 μm. However, the flux increases by a factor of 1.8 in flight F735, while the altitude is constant across two-thirds of the observations with a climb of 2000 ft and 1000 ft at the beginning and end of the 2.5 hr of observations. The expected PWV for flight F735 also decreases by a factor 1.8 during the observations (Figure 4, top) and shows a bump at approximately halftime of the observations. This behavior causes an increase in flux and a bump in

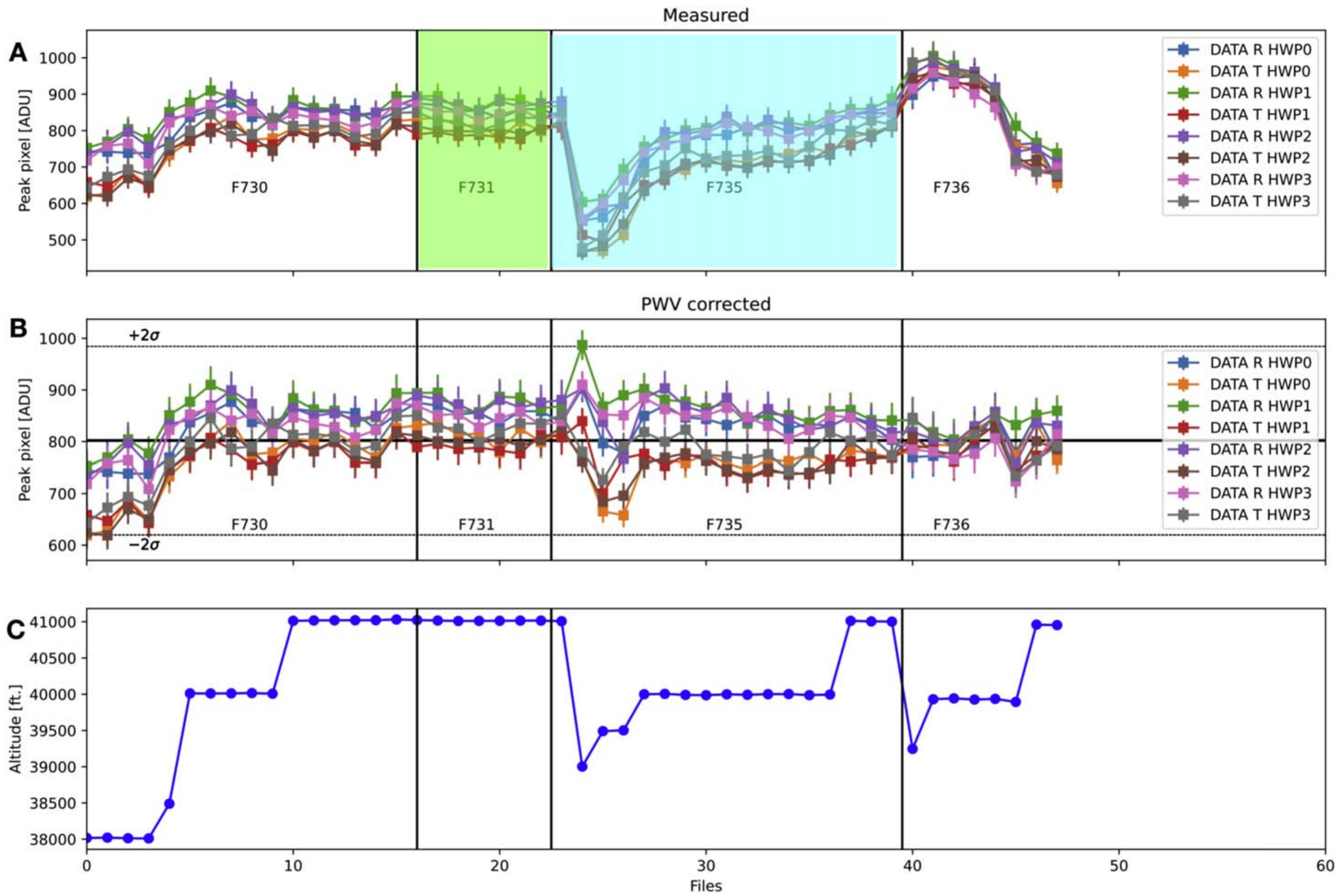

Figure 3. Flux variation and aircraft altitude as a function of time for the observations of M83 at 154 μm. (a) Measured peak fluxes of the scans per HWP PA and $\mathcal{R}$ and $\mathcal{T}$ arrays. (b) PWV-corrected fluxes using the fits shown in Figure 5. The mean (black solid line) and 2σ uncertainty (black dotted line) are shown. (c) Aircraft altitude at the time of data acquisition. The PWV during the observations of M83 (green for F731 and cyan for F735 shadowed regions) is shown in Figure 4.

the flux measured by HAWC+, which is in agreement with the measured fluxes and the factor of the increased fluxes (Figure 3(a) vs. Figure 4, top, as well as Figure 5).

We correct the PWV variations for each flight as follows. Fluxes for flights F735 and F736 were fitted with a polynomial function of order 3 and rescaled to the mean flux from flight F731. The left panel of Figure 5 shows the measured (uncorrected) fluxes with the fitted polynomial function. To conserve the relative contribution of the fluxes between $\mathcal{R}$ and $\mathcal{T}$ scans for each HWP PA per set, the polynomial function was fitted using all measured fluxes as shown in Figure 5. The fit was normalized to the mean measured flux from F731, which shows a constant flux within the flight at the highest altitude from the full set of observations. Finally, each measured flux from each set was multiplied by the normalization factor to correct for the PWV variation (Figure 5, right). Final corrected fluxes are shown in Figure 3(b). On average, fluxes vary by ∼15% across the full observations, with some outlier sets at ∼20%. The normalization to the mean flux of a flight with flux variations $\leqslant 10\%$ was selected; this approach minimized the flux calibration uncertainties to $< 20\%$ between flights. The same methodology was applied to NGC 6946 (Appendix A). At this stage, eight different images with positive background and corrected by PWV variations with a flux calibration uncertainty are computed $\leqslant 15\%$ (Figure 1, third row).

2.5. Stokes Parameters and Instrumental Polarization

The Stokes parameters *IQU* were estimated using the double difference method (equations shown in Figure 1) in the same manner as the standard C2N observations carried by HAWC+ described in Section 3.2 in Harper et al. (2018). In Figure 1, n is the number of sets, and $\mathcal{R}_\phi$ and $\mathcal{T}_\phi$ are the total intensity images of the $\mathcal{R}$ and $\mathcal{T}$ arrays per HWP PA. The IP was corrected using the polarization skydips. Specifically, the polarization skydips were performed by moving the telescope from 57° to 23° in elevation while the HWP rotates at a constant speed (Harper et al. 2018). These observations provide an estimate of the Stokes *qu* per detector pixel across the full array (Appendix B, Figure 14). The final IP was estimated as the weighted median of all pixels, and the associated uncertainty was estimated as the weighted standard deviation of the median. Figure 6 shows the estimated IP as a percentage of the normalized Stokes *qu* in the instrument reference frame. The numerical values and their uncertainties are shown in Table 3. We estimate an IP variation of $\leqslant 0.2\%$ across the FOV with a median IP of 1.6%–2.1% within the wavelength range of 53–214 μm.

For all galaxies, the IP was corrected by subtracting a constant Stokes *qu* from the measured Stokes *qu* of each galaxy. We use the normalized Stokes *qu* from the polarization skydips. The IP correction was performed in the instrument

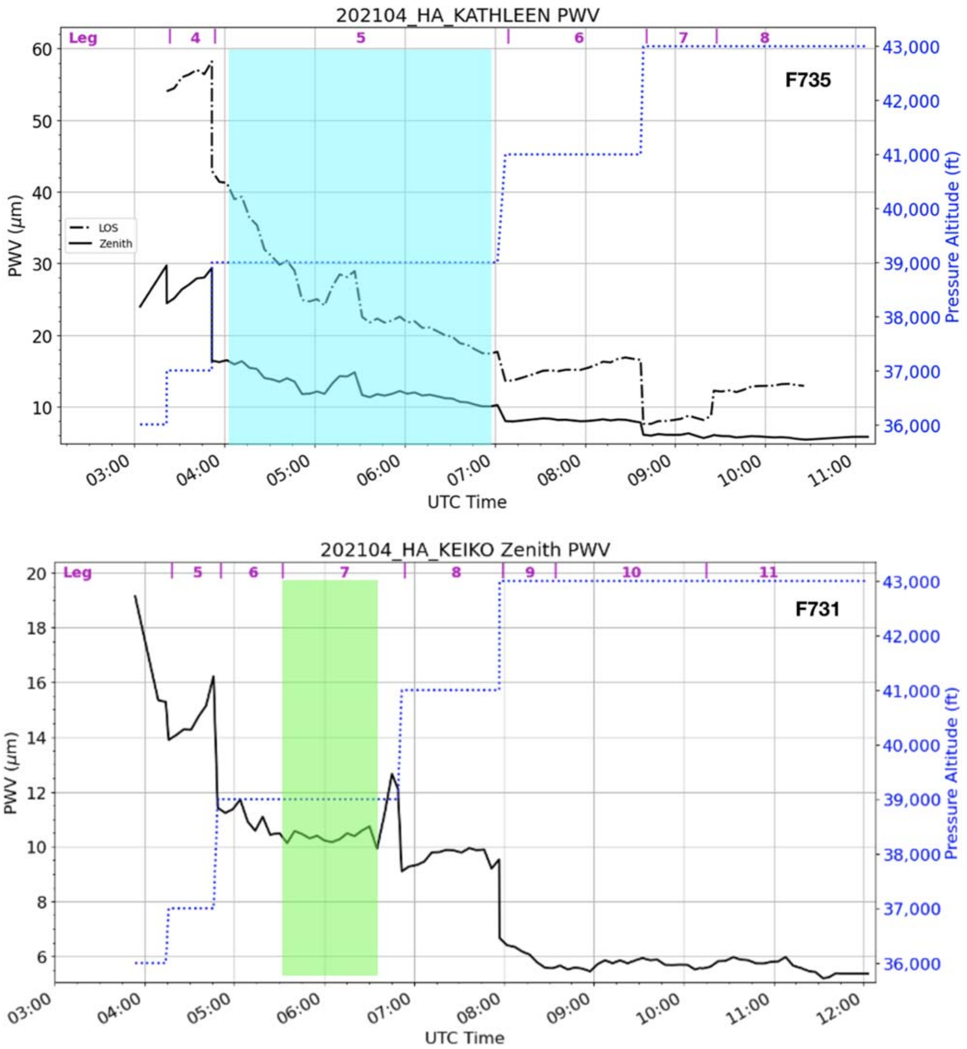

Figure 4. PWV variation as a function of time for the flights associated with M83 at 154 μm (see Figure 3). Top panel: expected PWV for flight F735. The PWV during the observations of M83 (cyan shadowed region) is shown. Bottom panel: expected PWV for flight F731. The PWV during the observations of M83 (green shadowed regions) is shown.

reference frame before the rotation to the sky coordinates. This correction has a polarization uncertainty of $\leqslant 0.2\%$ across the FOV in any band (Harper et al. 2018, and Section 3.3, Figure 14). We include an uncertainty of 0.2% in the polarization fraction in quadrature to the uncertainties estimated in the scientific analysis of this project. Finally, for each set, we rotate the Stokes *QU* from the instrument to the sky coordinates. At this stage, the Stokes *QU* corrected by IP are in sky coordinates for each set (Figure 1, fourth row).

To quantify the feasibility of our data reduction scheme, we performed OTFMAP polarimetric observations of planets (i.e., Neptune and Uranus) in all bands during 2021. We reduced these observations using the same approach as described above. Specifically, for each set of four HWP PAs, we reduced the raw data before estimating the Stokes *IQU* images. Then, Stokes *QU* were normalized such that $q = Q/I$ and $u = U/I$. We computed the median and standard deviation of q and u within the beam size centered at the peak intensity of Stokes I for each band. The final IP was estimated as the weighted median of all measurements, and the associated uncertainty was estimated as the weighted standard deviation of the median. As an example, Appendix B (Figure 15) shows the Stokes I and normalized Stokes qu for Neptune at 53 μm. The central beam (white circle) used to estimate the Stokes parameters is shown. After we apply the same IP correction to the planets, we estimate a residual polarization of $\leqslant 0.3\%$.

2.6. Flux Calibration and Data Merging

The flux is calibrated using observations of standard sources (i.e., planets, asteroids). The SOFIA Science Center routinely observes standard sources through each observing run and derives the flux calibration factors to be applied to each band. Harper et al. (2018) describe the flux calibration processes in more detail. We used the standard flux calibration factors (associated uncertainties are $\leqslant$15%) provided by the SOFIA Science Center for each observation. At this stage, Stokes *IQU* in sky coordinates for each set are flux-calibrated (Figure 1, fifth row).

Multiflight and multicycle observations were merged. Stokes *IQU* were merged using an adaptive weighted average[19] within a common grid with a specified pixel size, where north is up and east is left. The pixelization of this grid (i.e., final data

---

[19] A detailed description of the adaptive weighting algorithm used by SOFIA can be found at https://sofia-usra.github.io/sofia_redux/sofia_redux/toolkit/resampling/parameters.html#adaptive-weighting.

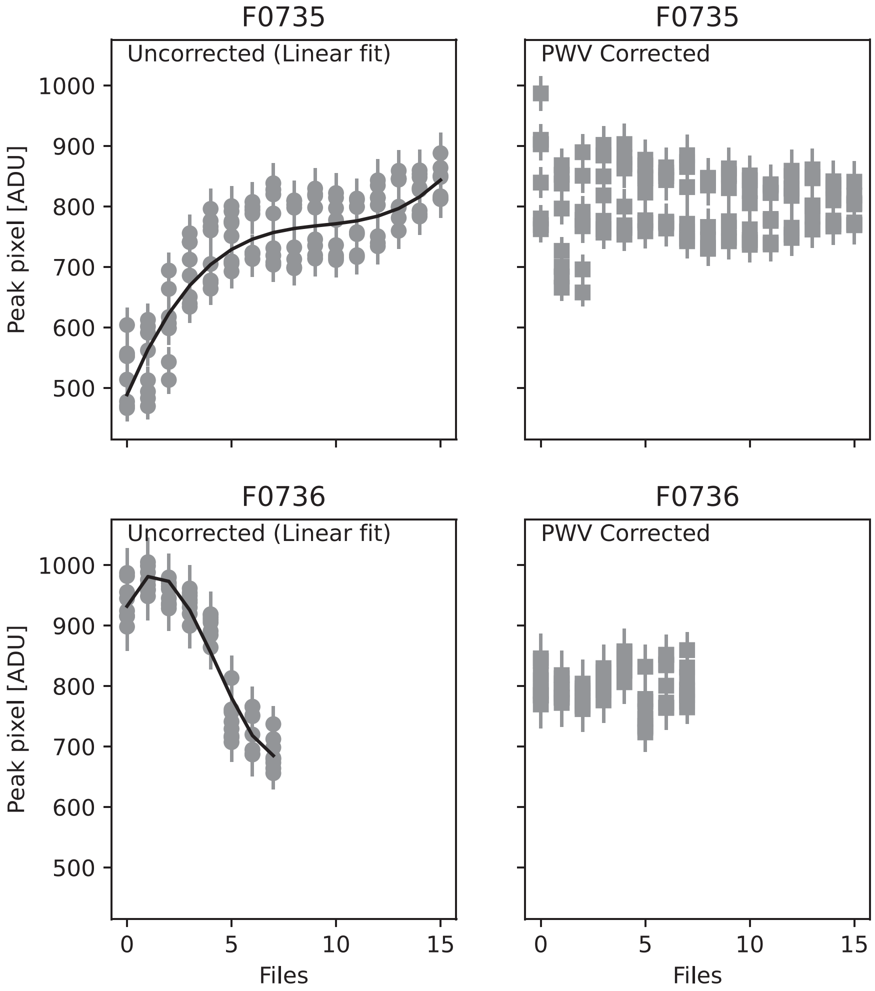

Figure 5. Fluxes uncorrected and corrected owing to PWV variations during observations of M83. Measured fluxes (left column) are fit with a polynomial function of order 3 (black solid line) for flights F0735 (top) and F0736 (bottom). Corrected fluxes (left column) by the normalized fit to the mean flux of flight F731 are shown.

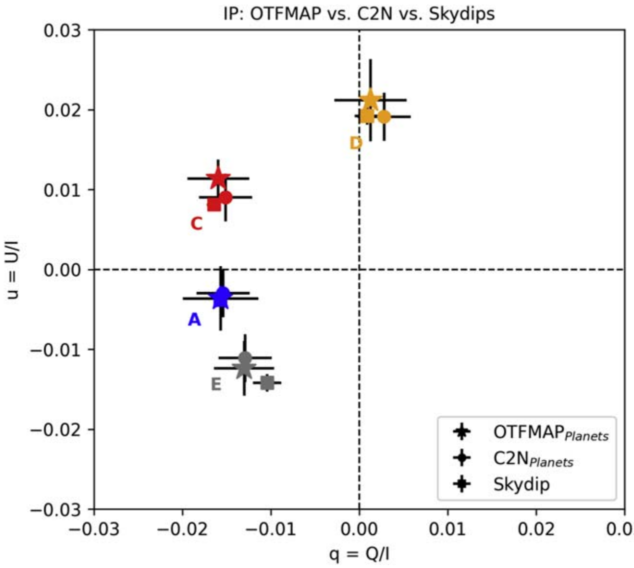

Figure 6. IP for the C2N and OTFMAP observing modes at all bands. IP for the C2N (circles), OTFMAP (stars), and polarization skydips (squares) for bands A (blue), C (red), D (orange), and E (gray) are shown. Definitions and details of the estimation of the IP are described in Sections 2.5 and 3.3.

product) is set to match the detector pixel size in a given band (Table 2), a value equivalent to Nyquist sampling. For each pixel, the weighted average within the FWHM of the associated band is estimated. Thus, the final data product has a Nyquist sampling pixelization with correlated fluxes within the FWHM of the band. The error maps are estimated from the input variances for the pixels involved in each weighted average.

The polarization fraction, P, position angle of polarization, PA, and polarized intensity, PI, are derived from the merged Stokes IQU. The polarization fraction is then debiased, $P' = \sqrt{P^2 - \sigma_p^2}$, and corrected for polarization efficiency, $P'' = P'/P_{\rm eff}$, where σ_p is the polarization uncertainty, and $P_{\rm eff}$ is the fractional polarization efficiency of 0.842, 0.939, 0.975, and 0.978 at 53, 89, 154, and 214 μm, respectively. HAWC+ has an absolute error of 3° in polarization angle and 0.4% in polarization fraction (Harper et al. 2018).

Final Stokes I values were spatially cross-correlated with PACS/Herschel images at the closest wavelength to correct the WCS of the HAWC+ images. Small corrections of 1–2 pixels were required for all HAWC+ observations to match with the central core of the galaxies observed with Herschel. These small offsets were applied to the maps of the Stokes IQU, P, PA, PI, and their associated uncertainties. At this stage, Stokes

Table 3
Instrumental Polarization from OTFMAP, C2N, and Skydips

Band	OTFMAP		C2N		Skydips	
	q (%)	u (%)	q (%)	u (%)	q (%)	u (%)
(1)	(2)	(3)	(4)	(5)	(6)	(7)
	2021[a]		2017		Oct−Nov 2017	
A	−1.57 ± 0.43	−0.36 ± 0.40	−1.54 ± 0.30	−0.30 ± 0.30	−1.60 ± 0.07	−0.38 ± 0.02
C	−1.59 ± 0.35	1.14 ± 0.24	−1.51 ± 0.30	0.90 ± 0.30	−1.64 ± 0.08	0.82 ± 0.07
D	0.13 ± 0.41	2.12 ± 0.52	0.28 ± 0.30	1.91 ± 0.30	0.14 ± 0.14	1.89 ± 0.11
E	−1.30 ± 0.34	−1.24 ± 0.34	−1.29 ± 0.30	−1.11 ± 0.30	−1.09 ± 0.16	−1.41 ± 0.11

Notes. Column (1): band name. Column (2): percentage Stokes *qu* for the OTFMAP observing mode. Column (3): percentage Stokes *qu* for the C2N observing mode. Column (4): percentage Stokes *qu* for polarization skydips.

[a] The year in which the data were obtained, with polarization measured using one of the three listed techniques.

IQU, *P*, PA, and PI values and their associated uncertainties are computed and ready for scientific analysis (Figure 1, sixth row).

2.7. Data Products

The data products generated within this data release are publicly available on the SOFIA Legacy Program website via http://galmagfields.com/. The database contains 14 galaxies observed at multiple wavelengths as shown in Table 4. A total on-source time of 47.54 hr (51.34 hr including overheads) is presented, which corresponds to 33% of the total awarded time of 155.70 hr (including overheads) for this SOFIA Legacy Program. An additional 11.84 hr (including overheads) of observations for Centaurus A (Lopez-Rodriguez 2021), Circinus, M51 (Borlaff et al. 2021), and NGC 1097 (Lopez-Rodriguez et al. 2021) are included in this data release. Each file contains Stokes *IQU*, *P*, PA, and PI values and their associated uncertainties with a pixel scale equal to the half-beam size for a given band. The released files have the same file format as Table 2 of Gordon et al. (2018).

In this manuscript, we focus on the characterization of the new observing technique and show the overall status of the observations and the polarization maps of each object. A detailed quantitative analysis of the polarization fraction and magnetic field orientation will be presented in Papers IV (Lopez-Rodriguez et al. 2022) and V (in preparation) of the series. Figures 7, 8, and 9 show the polarization maps of the released data. Polarization measurements are shown with a constant length to display the magnetic field orientation. The polarization measurements (*E*-vector) were rotated by 90° to show the *B*-field orientation. We selected polarization measurements with $P/\sigma_P \geqslant 3$, $\mathrm{PI}/\sigma_{\mathrm{PI}} \geqslant 3$, $P \leqslant 30\%$, and $I/\sigma_I \geqslant 80$ for all galaxies, where σ_I and σ_{PI} are the uncertainties in Stokes *I* and polarization intensity, respectively.

Table 4
Status of Released Galaxy Sample

Galaxy (1)	Band (μm) (2)	Requested Time[a] (h) (3)	Observed Time[a] (h) (4)	Completed[b] (5)
Centaurus A	89	⋯	0.89	⋯
Circinus	53	⋯	0.11	⋯
	89	⋯	0.89	⋯
	214	⋯	0.29	⋯
M51	154	⋯	2.78	⋯
M82	53	2.00	1.60	✓
	89	2.00	1.65	✓
	154	2.00	1.99	✓
	214	2.00	1.13	✓
M83	154	6.80	6.60	✓
NGC 253	89	3.00	1.00	33%
	154	5.00	0.89	18%
NGC 1068	53	3.07	1.06	35%
	89	7.07	2.00	28%
NGC 1097	53	⋯	1.87	⋯
	154	⋯	0.27	⋯
NGC 2146	53	3.00	1.60	53%
	89	3.00	2.02	67%
	154	3.00	2.40	80%
	214	3.00	2.33	✓
NGC 3627	154	6.80	4.53	67%
NGC 4736	154	6.80	2.22	33%
NGC 4826	89	6.80	1.22	18%
NGC 6946	154	6.80	7.20	✓
NGC 7331	154	6.80	6.10	✓

Notes. Column (1): galaxy name. Column (2): central wavelength of the band. Column (3): on-source requested time. Column (4): observed on-source time. Column (5): completed fraction per object per band.

[a] On-source times. Overhead of 1.08 for OTFMAP observations (Table 5), except for M51 with a specific overhead of 2.59 for C2N observations. Observations from other SOFIA programs are shown with ellipsis points.

[b] The final observations are considered as completed (i.e., ✓) when (a) completion >85% or (b) a desired S/N was reached. Observations from other SOFIA programs are shown with ellipsis points.

3. OTFMAP and C2N Comparison

This section shows a quantitative comparison of the overheads, sensitivities, and IP between the C2N and OTFMAP observation modes of HAWC+.

3.1. Observing Overheads

The OTFMAP observational strategy for polarimetry has been described in Section 2.2.1. Here we briefly describe the specifics of the C2N polarimetric observations using HAWC+ (for further details see Harper et al. 2018). The telescope with the secondary mirror on the optical axis points to the science object. Then, the secondary mirror is moved at a frequency of 10.2 Hz between the science object and an adjacent position on the sky. This movement is characterized by its amplitude (i.e., chop throw) and direction (i.e., chop angle). Each pair of science and sky images is subtracted to eliminate the background emission from the science image. To minimize the radiative offset, the telescope is moved every 30–50 s

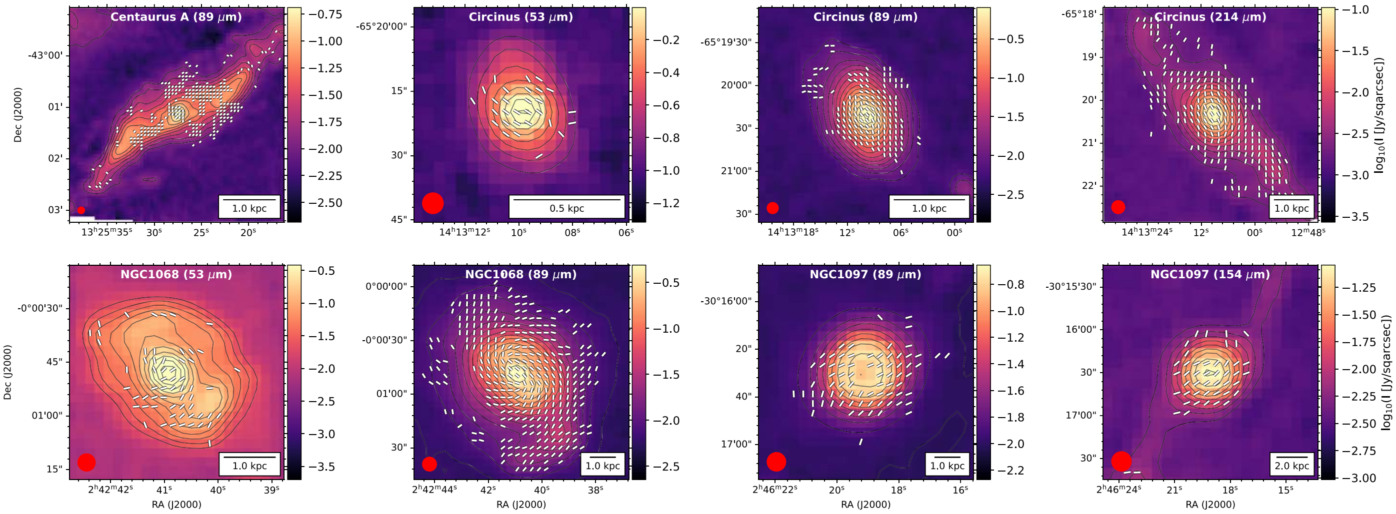

Figure 7. Active galactic nuclei. Shown are Centaurus A at 89 μm; Circinus at 53, 89, and 214 μm; NGC 1068 at 53 and 89 μm; and NGC 1097 at 89 and 154 μm. Also shown is total intensity (color scale) in logarithmic scale with contours increasing in steps of $2^n\sigma$, with $n = 5, 5.5, 6,...$. The measurements of polarization fraction (white lines) are shown with constant length to display the B-field orientations. Only measurements of polarization fraction with $P/\sigma_P \geqslant 3$ and $I/\sigma_I \geqslant 80$ were selected. A physical scale (black line) of 0.5, 1.0, or 2.0 kpc and the beam size (red circle) are shown.

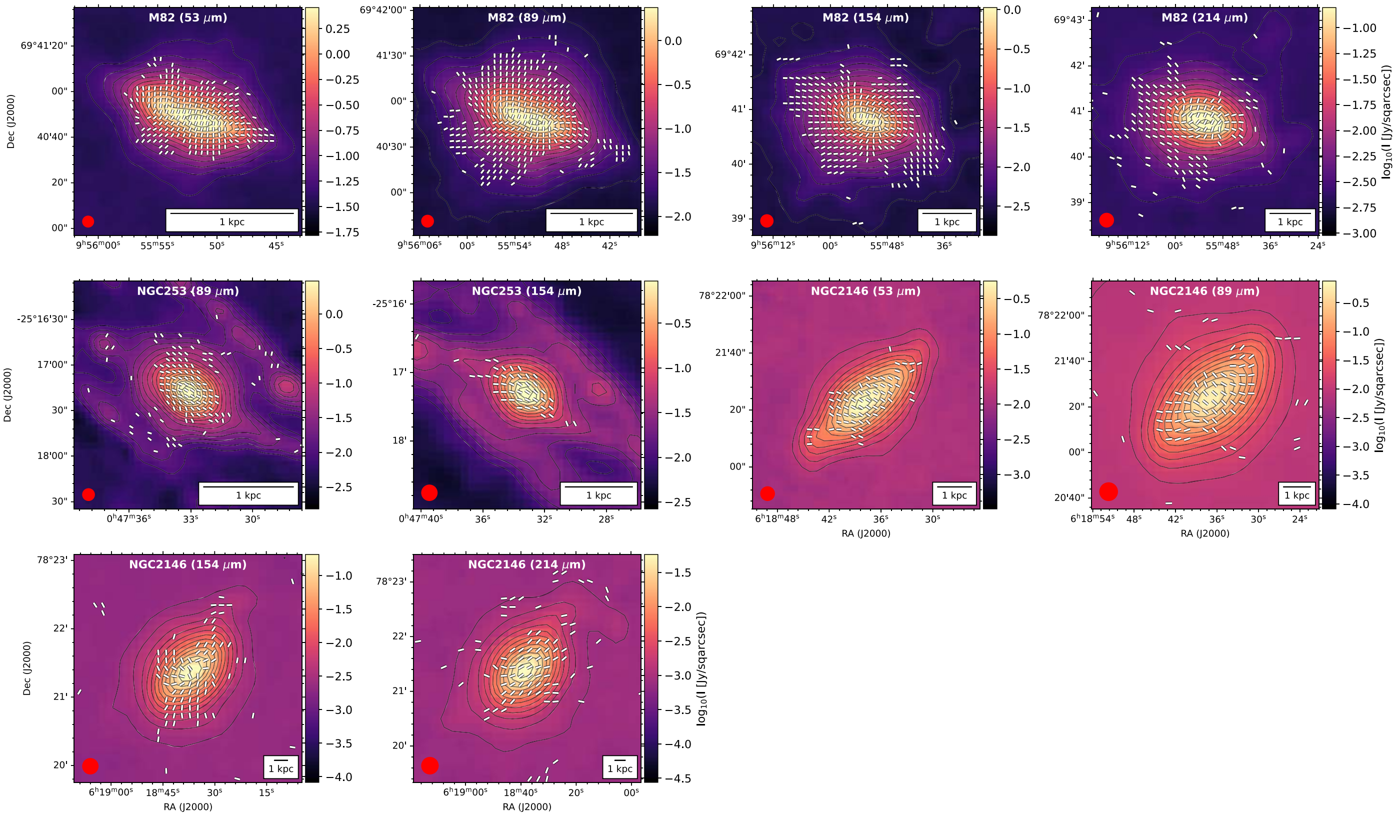

Figure 8. Starburst galaxies. Shown are M82 at 53, 89, 154, and 214 μm; NGC 2146 at 53, 89, 154, and 214 μm; and NGC 253 at 89 and 154 μm. Total intensity (color scale) is shown in logarithmic scale with contours increasing in steps of $2^n\sigma$, with $n = 5, 5.5, 6,...$. The measurements of polarization fraction (white lines) are shown with constant length to display the B-field orientations. Only measurements of polarization fraction with $P/\sigma_P \geqslant 3$ and $I/\sigma_I \geqslant 80$ were selected. A physical scale (black line) of 1.0 kpc and the beam size (red circle) are shown.

(i.e., nod time) with the same amplitude and direction as the chop. Asymmetric chop-nod is not performed with HAWC+ owing to the associated large overheads. The final image is computed after a pair of subtracted chop-nod observations, which produces a positive image of the science object at the location of the boresight within the FOV of HAWC+. Chopping within the array is not performed owing to the small FOVs (Table 2). This procedure is repeated per HWP PA in a sequence of 5°, 50°, 27.°5, and 72.°5. As the yield of operational detectors is ~70% (Harper et al. 2018), these sets of observations are repeated in a four-point dither sequence with a 3-pixel offset around the boresight in a given HAWC+ band. Before and after the sequence of four HWP PAs, internal calibration images (i.e., INTCAL) of 15 s each are taken to

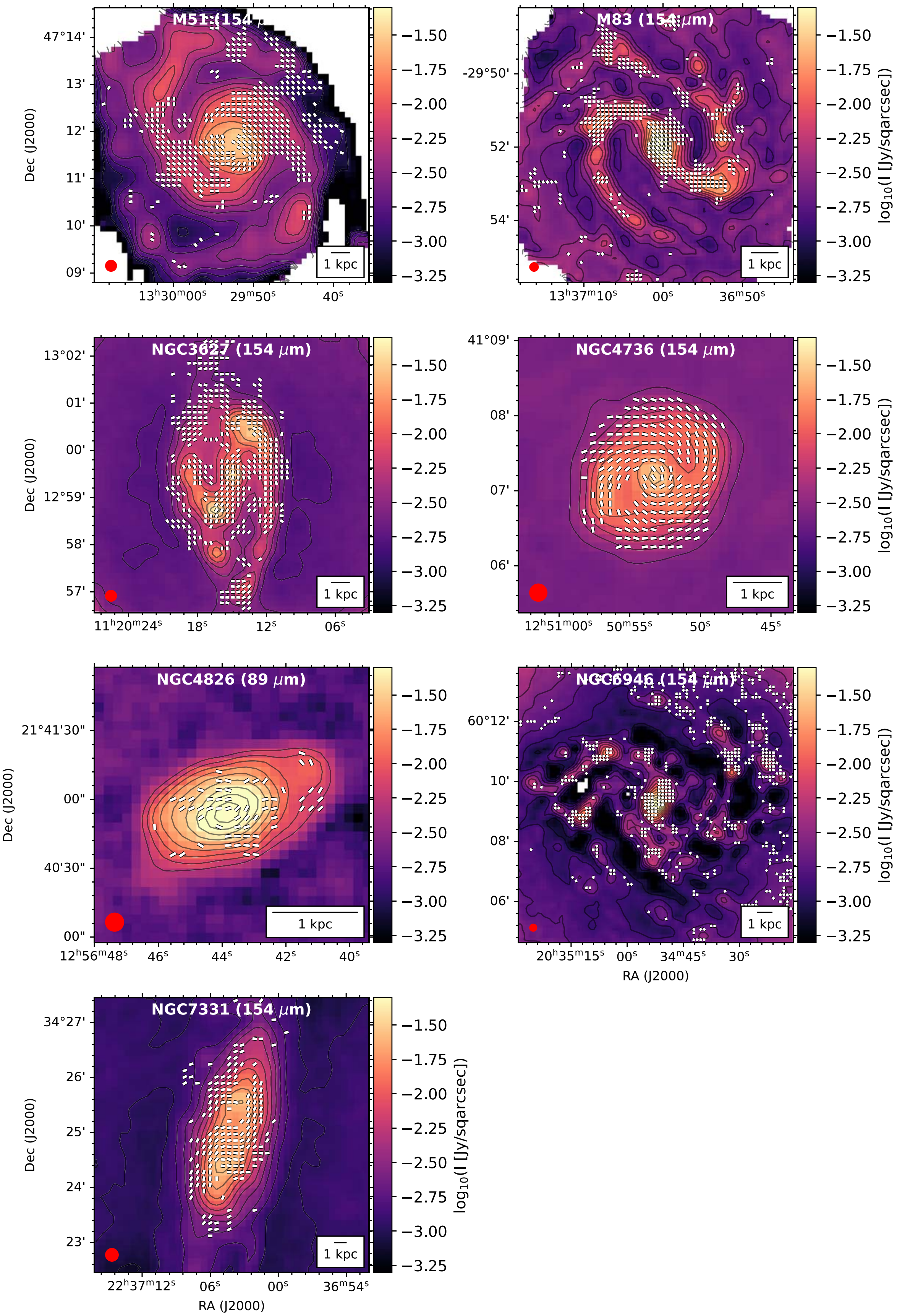

Figure 9. Spiral galaxies. M51, M83, NGC 3627, NGC 4736, NGC 6946, and NGC 7331 at 154 μm and NGC 4826 at 89 μm are shown. Total intensity (color scale) is shown in logarithmic scale with contours increasing in steps of $2^n\sigma$, with $n = 5, 5.5, 6,\ldots.$ The measurements of polarization fraction (white lines) are shown with constant length to display the B-field orientations. Only measurements of polarization fraction with $P/\sigma_P \geqslant 3$ and $I/\sigma_I \geqslant 80$ were selected. A physical scale (black line) of 1.0 kpc and the beam size (red circle) are shown.

calibrate the C2N observations and compute observing flat-fields.

The total observing time for the C2N polarimetric mode is estimated using the start and end time of observations for each file, and the total on-source times are computed as

$$t_{\text{on-source,C2N}} = \frac{\text{nodtime}}{2} \times n_{\text{dithers}} \times n_{\text{HWPPAs}}, \quad (1)$$

where nod time is the nodding time where half of the time is spent on the science object, n_{dithers} is the number of dither positions, and n_{HWPPAs} is the number of HWP PAs.

The total on-source time for the OTFMAP polarimetric mode is estimated as

$$t_{\text{on-source,OTFMAP}} = t_{\text{ScanDuration}} \times n_{\text{HWPPAs}}, \quad (2)$$

where $t_{\text{ScanDuration}}$ is the scan duration per scan as shown in Table 1.

We compare the observing overheads of the C2N and OTFMAP polarimetric observations of NGC 1068 and Circinus at 89 μm. The C2N observations of NGC 1068 were presented by Lopez-Rodriguez et al. (2020) with a total observing time of 7615 s and a total on-source time of 2910 s. The chop throw is 180″, and the chop angle is 90° to always be along the short axis of the array. The C2N observations of Circinus were performed during the same flight, F596, as those of the OTFMAP polarimetric observations with a total observing time of 615 s and a total on-source time of 252 s. The chop throw is 180″, and the chop angle is 322° counterclockwise in the east of north direction.

A subgroup of the OTFMAP observations presented in Table 1 were reduced to have on-source times similar to the C2N observations. OTFMAP polarimetric observations with an on-source time of 2880 and 400 s were reduced following the steps described in Section 2 for NGC 1068 and Circinus, respectively. The associated total observing times of these subsets of observations are 3041 and 428 s for NGC 1068 and Circinus, respectively. Figures 10 and 15 show the C2N configuration and Lissajous curves from one of the scans over the Herschel image at 70 μm for NGC 1068 and Circinus, respectively.

The observing overhead factor for the C2N observing mode is estimated to be 2.53, while an observing overhead of 1.08 is estimated for the OTFMAP observing mode (Table 5). Then, the total observing time is computed as

$$t_{\text{C2N}} = 2.53 \times t_{\text{on-source,C2N}} \quad (3)$$

$$t_{\text{OTFMAP}} = 1.08 \times t_{\text{on-source,OTFMAP}}. \quad (4)$$

The OTFMAP overhead arises from (a) the time spent to rotate the four HWP PA and (b) the waiting time of ∼2–4 s to ensure that tracking is correctly performed between scans. The C2N overhead arises from (a) chopping on the sky positions and nodding the telescope, (b) INTCALs of 15 s each before and after the sequence of four dither positions, and (c) the rotation of the HWP PAs. We estimate that the OTFMAP polarimetric mode provides a total improvement in observing time overhead of a factor of 2.53/1.08 = 2.34 with respect to the C2N polarimetric observations. The main reason for this improvement is that the galaxies are always within the FOV of the HAWC+ array during the whole integration time.

3.2. Sensitivities

The sensitivities of the total intensity mode using OTFMAP and polarimetry mode using C2N have been already characterized (Harper et al. 2018). We present the sensitivity estimations of the OTFMAP polarimetric mode at 89 μm (Band C) as an example of the improvement provided by this new observing mode. Further characterization in different bands will be performed and released by the SOFIA Science Center. The SOFIA observer's handbook for HAWC+[20] defines the sensitivities as follows: the Minimum Intensity flux for Polarimetry (MIfP) is given as the flux needed to reach 0.3% polarization uncertainty in 3600 s for an extended source, and the Minimum Detectable Continuum Polarized Flux (MDCPF) is given as the total flux needed to reach a 4σ detection assuming a source with a polarization fraction of 1% in 900 s of on-source time for point sources.

Using the OTFMAP and C2N polarimetric observations of NGC 1068 and Circinus at 89 μm, Figures 10 and 15 clearly show an increase in the number of polarization measurements with the same statistical significance (i.e., $P/\sigma_P \geqslant 3$) and a larger spatial extension of the polarized flux with the same $\text{PI}/\sigma_{\text{PI}} \geqslant 3$. Figures 11 and 16 show the histograms of the total and polarized fluxes, as well as a 1:1 plot between the polarization fraction and polarization angle for NGC 1068 and Circinus, respectively. For the 1:1 plot, measurements associated with the same WCS were plotted. We estimate a standard deviation of 9°.8 for the polarization angle between C2N and OTFMAP observing modes, which is compatible with the angular dispersion of 9°.5 associated with polarization measurements with a $P/\sigma_P = 3$. The largest angular differences arise from the low S/N ratio polarization measurements colocated with the extended diffuse emission in the northern and southern regions. We conclude that the Stokes I, PI, P, and PA are total flux, polarized flux, polarization fraction, and position angles are in agreement between both OTFMAP and C2N polarimetric observations. In addition, after the standard deviation of the observations is normalized using their associated on-source time, we find that the standard deviation of the polarized flux decreases for the OTFMAP polarimetric observations (middle right panels of Figures 11 and 16), demonstrating a significant improvement in sensitivity by the OTFMAP polarimetric mode.

Using the observing overheads presented in Section 3.1, we estimate an MIfP of 7010 MJy sr^{-1} and an MDCPF of 59% Jy in C2N mode at 89 μm. These values are in agreement, within the nominal 20% flux uncertainty, with the quoted MIfP of 6000 MJy sr^{-1} and MDCPF of 50% Jy by Harper et al. (2018) and the HAWC+ observer's handbook. The estimated MIfP and MDCPF for the OTFMAP polarimetric mode are shown in Table 5. Finally, we estimate a sensitivity improvement of 1.80 in MIfP, for the same on-source time between the OTFMAP and C2N polarimetric modes. As mentioned in the introduction, an increase of a factor of $\sqrt{2}$ was expected owing to a single pointing at the on-axis position by the OTFMAP. Our approach provides an improvement of a factor $\sqrt{1.8}$ from the theoretical $\sqrt{2}$, ∼5% ($\sqrt{1.8}/\sqrt{2} = 0.95$) lower than expected. This difference may be due to systematic effects within the OTFMAP that may be improved following some of the suggestions described in Section 3.4. After accounting for

---

[20] Observer's Handbook for HAWC+ can be found at https://www.sofia.usra.edu/instruments/hawc.

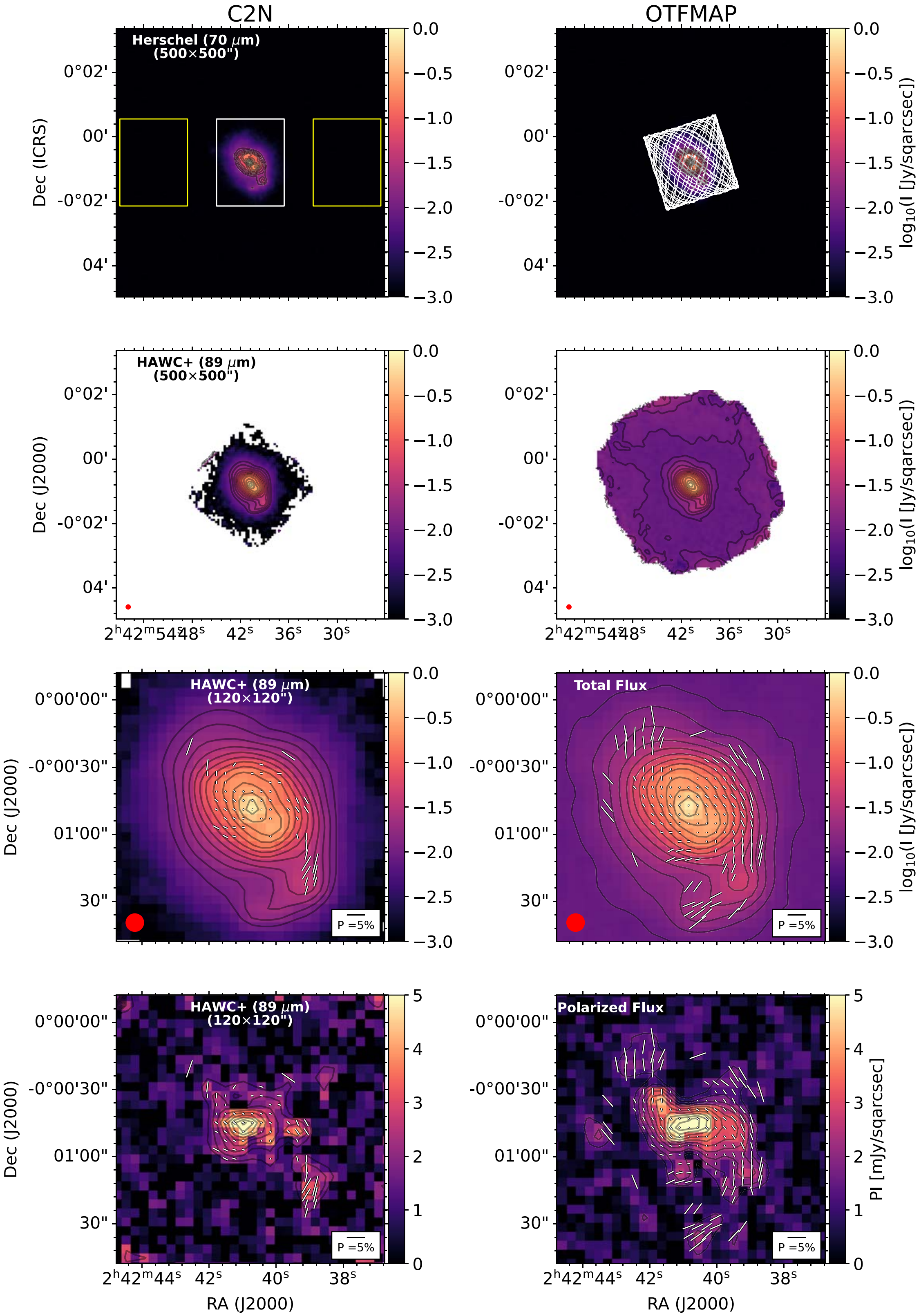

Figure 10. Comparison between C2N (left) and OTFMAP (right) observations of NGC 1068 at 89 μm. First row: Herschel observations at 70 μm (color scale) of NGC 1068 within an FOV of 500 × 500 arcsec^2 with overlaid C2N (left) and OTFMAP (right) configurations. For C2N, on-axis (white) and off-axis (yellow) positions with the FOV of HAWC+ at 89 μm are shown. For OTFMAP, the Lissajous curve (white solid line) of one scan is shown. Second row: HAWC+ total flux observations for C2N and OTFMAP within the same FOV as above. Contours start at $32\sigma_I$ and increase in steps of $2^n\sigma$, where $n = 5, 5.5, 6,...$ and $\sigma_I = 0.3$ mJy arcsec^{-2}. The beam size is shown as a red circle in the lower left corner. Third row: same as above within an FOV of 120 × 120 arcsec^2. Polarization measurements (white lines) are shown for $P/\sigma_P \geqslant 3$, $\mathrm{PI}/\sigma_{\mathrm{PI}} \geqslant 3$, $P < 30\%$, and $I/\sigma_I \geqslant 50$. A 5% polarization measurement is shown at the bottom right. Fourth row: HAWC+ polarized flux observations (color scale) within the same FOV and polarization as above. Contours start at $3\sigma_{\mathrm{PI}}$ and increase in steps of $1\sigma_{\mathrm{PI}}$, where $\sigma_{\mathrm{PI}} = 0.46$ mJy arcsec^{-2}.

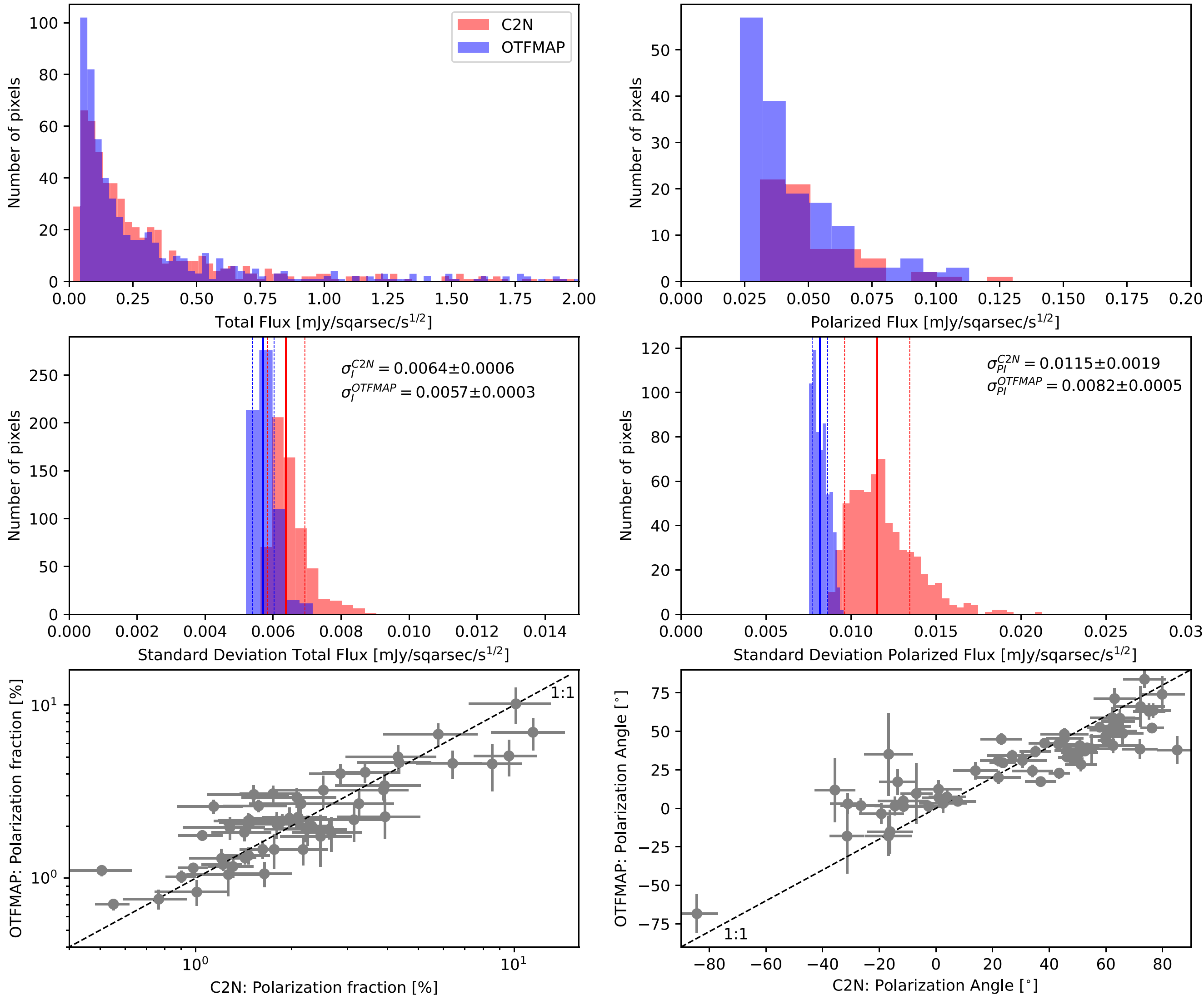

Figure 11. Sensitivity comparison between C2N (red) and OTFMAP (blue) observations of NGC 1068 at 89 μm. Histograms of the total intensity (top left), polarized intensity (top right), standard deviations of the total flux (middle left), and polarized flux (middle right) are shown. The median and 1σ uncertainty of the distribution of the standard deviations are shown in the middle panels. The polarization fraction (bottom left) and polarization angle (bottom right) for C2N and OTFMAP observations are shown. A 1:1 line (black dashed line) is shown.

Table 5

OTFMAP versus C2N: Overheads and Sensitivities Using Observations of Circinus and NGC 1068 at 89 μm

Obs. Mode	Overhead	With Overheads		Without Overheads	
		MIfP[b] with $\sigma_p = 0.3\%$ in 3600 s (MJy sr^{-1})	MDCPF[b] with 4σ in 900 s (% Jy)	MIfP with $\sigma_p = 0.3\%$ in 3600 s (MJy sr^{-1})	MDCPF with 4σ in 900 s (% Jy)
(1)	(2)	(3)	(4)	(5)	(6)
C2N	2.53	7010	59	4333	37
OTFMAP	1.08	2819	21	2410	21
Improvement$_{OTFMAP}$[a]	2.34	2.49	2.81	1.80	1.76

Notes. Column (1): observing mode. Column (2): observing time overhead (i.e., total exposure time/on-source time). Column (3): minimum intensity flux for polarimetry (MIfP) to achieve a polarization uncertainty of 0.3% in 3600 s (including overheads). Column (4): minimum detectable continuum polarized flux (MDCPF) for a 4σ detection assuming a source with a polarization fraction of 1% in 900 s (including overheads). Column (5): same as Column (3), but only taking into account on-source time. Column (6): same as Column (4), but only taking into account on-source time.

[a] Improvement of the OTFMAP shown as a ratio between OTFMAP and C2N of the quantities shown for each column.

[b] Harper et al. (2018) quote an MIfP and MDCPF, including overheads, of 6000 MJy sr^{-1} and 50% Jy, respectively.

observing time overheads, the OTFMAP polarimetric mode offers total improvement in MIfP of 2.49 times over the C2N observing mode.

3.3. Instrumental Polarization

The IP was estimated with unpolarized standard objects using C2N, OTFMAP, and polarization skydips. The IP from C2N and polarization skydips were collected in 2017 and computed by Harper et al. (2018). The polarizations from OTFMAP of planets were presented and computed in Section 2.5. Figure 6 shows the estimated IP as a percentage of the normalized Stokes *qu* in the instrument reference frame for the C2N, OTFMAP, and polarization skydips. The numerical values and their uncertainties are shown in Table 3. We find that all three methods produce consistent and reproducible results. The uncertainties are larger in C2N and OTFMAP than in the polarization skydips owing to the number of measurements used for the statistics. We take the measurements from the polarization skydips for the IP correction in our observations (Section 2.5).

We find a rotation in the IP with wavelength. The HAWC+ filters are metal grids (Harper et al. 2018), which probably introduce some level of intrinsic polarization. However, the polarization properties of these filters were not measured before they were installed in the instrument. The important result here is that the IP is reproducible and consistent throughout the different methods and the time and conditions of observations. The IP is known to arise from the tertiary mirror (Harper et al. 2018). Thus, our results show that the IP remains constant, within the uncertainties, from 2017 to 2021. This result suggests that the physical conditions of the tertiary mirror produce a negligible difference in IP during 5 yr of observations.

3.4. Further Implementations of the OTFMAP Polarization for HAWC+

Although we have shown that the OTFMAP polarimetric mode has substantially improved the overheads and sensitivities when compared to the C2N polarimetric mode, further developments on the OTFMAP polarimetric mode are still required. As mentioned above, the data processing presented in Section 2 works for objects with thermal emission within the FOV of HAWC+ in a given band. However, this procedure may not be as efficient for large-scale and diffuse thermal emission that covers areas much larger than the FOV of the HAWC+ array. This well-known deficiency of the OTFMAP observing mode can be mitigated by application of alternative OTFMAP strategies in the recovery of large-scale emission, as discussed below.

For FIR polarimetric observations, Hildebrand et al. (2000) suggested an observing strategy involving the telescope chopping to an adjacent sky location at the same time as scanning. As in C2N, the chop is then subtracted from the closest scan in time. While this technique may remove the sky fluctuations more efficiently than the procedure we presented earlier, it will increase the observing overheads and reduce the sensitivities, as there may be a residual radiative offset after the chop subtraction. Note that CRUSH has the option to reduce chop-scan observations with HAWC+; however, this observing mode has not been characterized. An alternative strategy consists of a continuous rotation of the HWP to modulate signal at a faster rate, usually ∼2 Hz, than the atmospheric fluctuations. Note that HAWC+ can continuously rotate the HWP to 0.5 Hz, providing a polarization modulation frequency of 2 Hz (Harper et al. 2018). The time streams for each pixel can then be linearly decomposed to IP, astrophysical polarization, detector gains, detector temperature fluctuations, and atmospheric transparency fluctuations. This technique is commonly used in submillimeter polarimetric observations, for example, by POL-2 on the James Clerk Maxwell Telescope (JCMT; Ward-Thompson et al. 2017), and cosmic microwave background (CMB) experiments (e.g., Johnson et al. 2007). FIR polarimetric observations using PolKa at APEX demonstrated the use of a rotating-wave plate, for which final data products were computed using CRUSH (Siringo et al. 2010, 2012). While this observing approach may be the most efficient, its implementation requires testing the software using HAWC+ observations and potentially new hardware development. These common issues are also well-known problems in radio polarimetric observations using scanning techniques. Müller et al. (2017) applied a technique called “basket-weaving” to map with orthogonal scanning on the sky, and Emerson & Graeve (1988) applied a technique called “PLAIT” for scans oriented at any angle. Although evaluating these observing modes is outside of the scope of this manuscript, we have mentioned them as options for future implementations that could reduce the observational overheads and, as a result, SOFIA’s operational cost.

4. Conclusions

We present the first data release (DR1) of the SOFIA Legacy program (PI: E. Lopez-Rodriguez & S. A. Mao) on extragalactic magnetism. The DR1 consists of 14 galaxies, including active galactic nuclei, starbursts, and spirals, from 53 to 214 μm, which constitutes 33% (51.43 hr out of 155.7 hr) of the total awarded time of this program. We release homogeneously reduced high-level data products, ready for scientific analysis.

We have presented the data processing of the OTFMAP polarization mode for HAWC+. The pipeline steps were applied to the newly acquired observations of galaxies from 2020 January to 2021 December within the SOFIA Legacy program on extragalactic magnetism. This new observing mode had been successfully applied to objects smaller than the FOV of the HAWC+ array in any given band. The data processing includes zero-level background subtraction, PWV correction, IP subtraction, and merging. Comparison with C2N observations shows that the OTFMAP has greatly improved the polarimetric mode of HAWC+. Specifically, we estimated that OTFMAP polarimetric mode provides an improvement in observing time overhead of a factor of 2.34 and an improvement of 1.80 in MIfP (i.e., sensitivity) for the same on-source time from the C2N polarimetric observations. Including these two factors, we estimate that the OTFMAP polarimetric mode offers a total improvement in MIfP of 2.49 times over the C2N observing mode. The OFTMAP is a significant optimization of the polarimetric mode of HAWC+, as it ultimately reduces the cost of operations of SOFIA/HAWC+; more data can be collected per hour of flight, more than doubling the number of programs/papers per hour of observation.

Although the polarimetric mode of HAWC+ has been improved, we emphasize that further development of this observing mode for objects with large-scale diffuse polarized emission is still required. We briefly described several observing strategies to improve this technique for HAWC+ based on the approaches from submillimeter observations and CMB experiments.

Based on observations made with the NASA/DLR Stratospheric Observatory for Infrared Astronomy (SOFIA) under the 07_0034, 08_0012 Program. SOFIA is jointly operated by the Universities Space Research Association, Inc. (USRA), under NASA contract NNA17BF53C, and the Deutsches SOFIA Institut (DSI) under DLR contract 50 OK 0901 to the University of Stuttgart. K.T. has received funding from the European Research Council (ERC) under the European Union's Horizon 2020 research and innovation program under grant agreement No. 771282. E.N. is supported by the ERC Grant "Interstellar" (grant agreement No. 740120) and has received funding from the Hellenic Foundation for Research and Innovation (H.F.R.I., project No. 224). S.M.A. is supported by the ERC starting grant 638707 "Black holes and their host galaxies: co-evolution across cosmic time" and by STFC.

Facilities: SOFIA (HAWC+), Herschel.

Software: ASTROPY (Astropy Collaboration et al. 2013), APLPY (Robitaille & Bressert 2012), MATPLOTLIB (Hunter 2007).

Appendix A
PWV Correction of NGC 6946

NGC 6946 shows flux variations in several flights owing to PWV fluctuations during the observations. Following the approach described in Section 2.4, the measured fluxes (Figure 12, top) were corrected by fitting a linear function (Figure 13) normalized to the mean fluxes of flights F684 and F685. The corrected fluxes (Figure 12, middle) show a flux variation of 15% across the full observations.

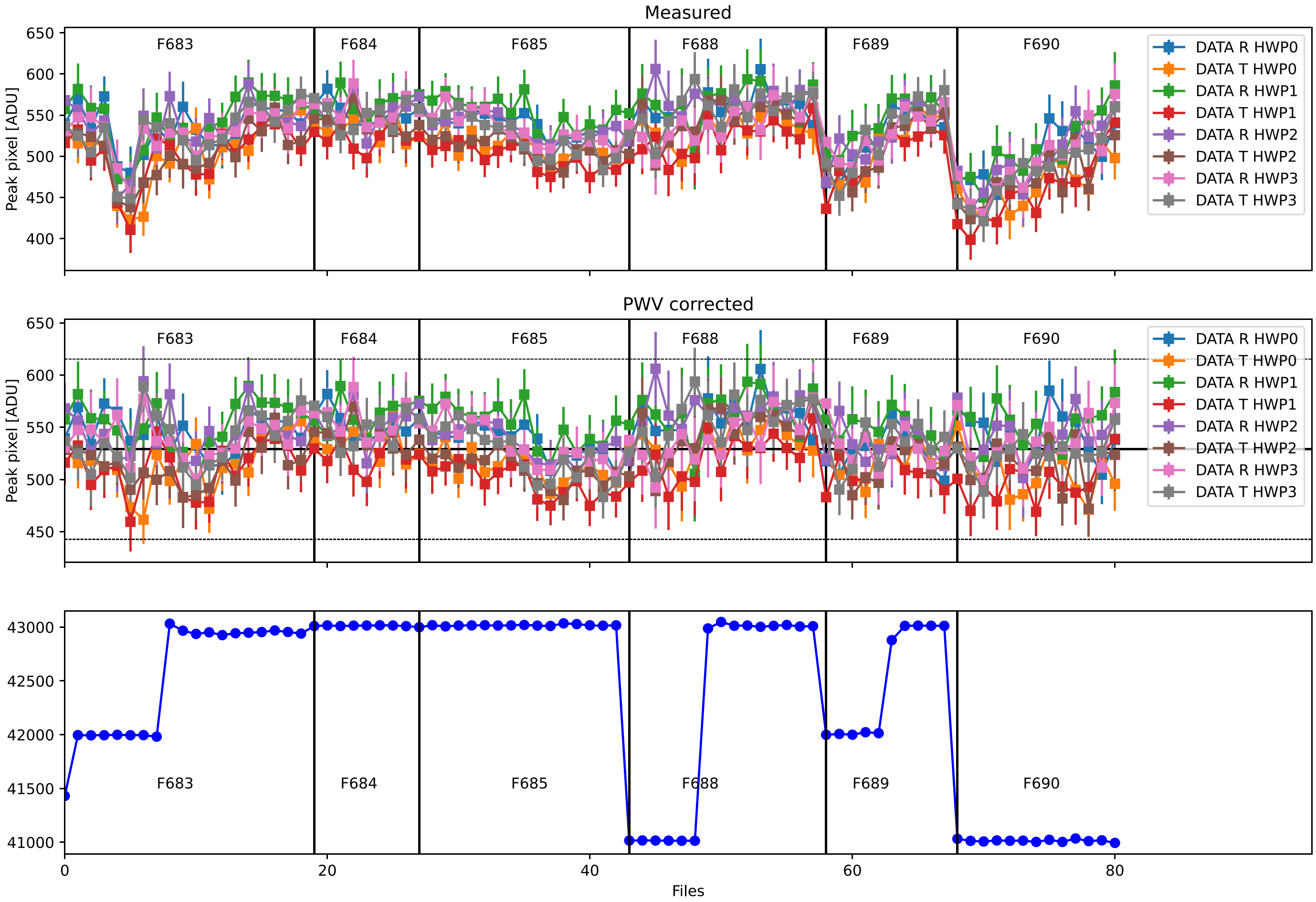

Figure 12. Flux variation as a function of time and aircraft altitude for NGC 6946 at 154 μm. Top panel: measured peak fluxes of the scans per HWP PA and $\mathcal{R}$ and $\mathcal{T}$ arrays. Middle panel: PWV-corrected fluxes using the fits shown in Figure 13. The mean (black solid line) and 2σ uncertainty (black dotted line) are shown. Bottom panel: aircraft altitude at the time of data acquisition.

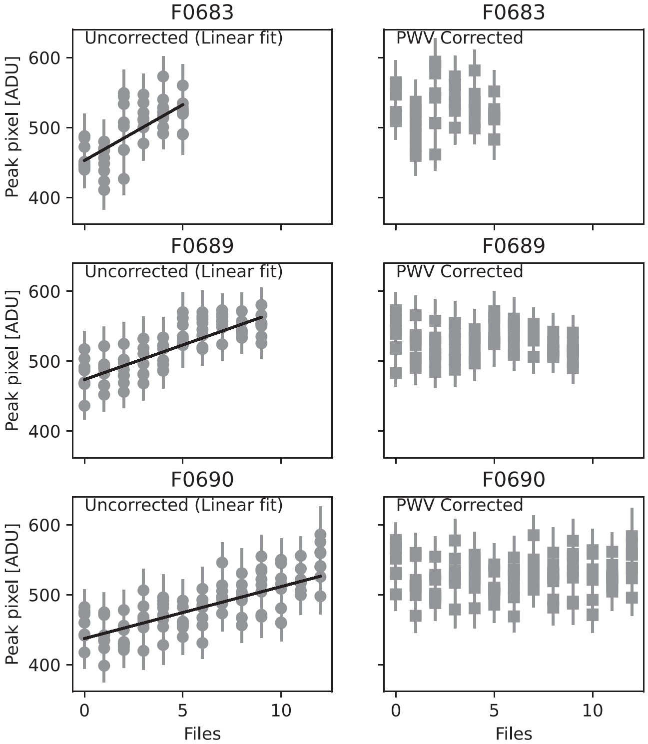

Figure 13. Fluxes uncorrected and corrected by a linear fit due to PWV variations during observations of NGC 6946. Measured fluxes (left column) are fit with a linear function (black solid line) for flights F0683 (top), F0689 (middle), and F0690 (bottom). Corrected fluxes (right column) by the normalized fit to the mean flux of flights F684 and F685 are shown.

Appendix B
Instrumental Polarization

This appendix shows the supporting figure (Figure 14) described in Sections 2.5 and 3.3.

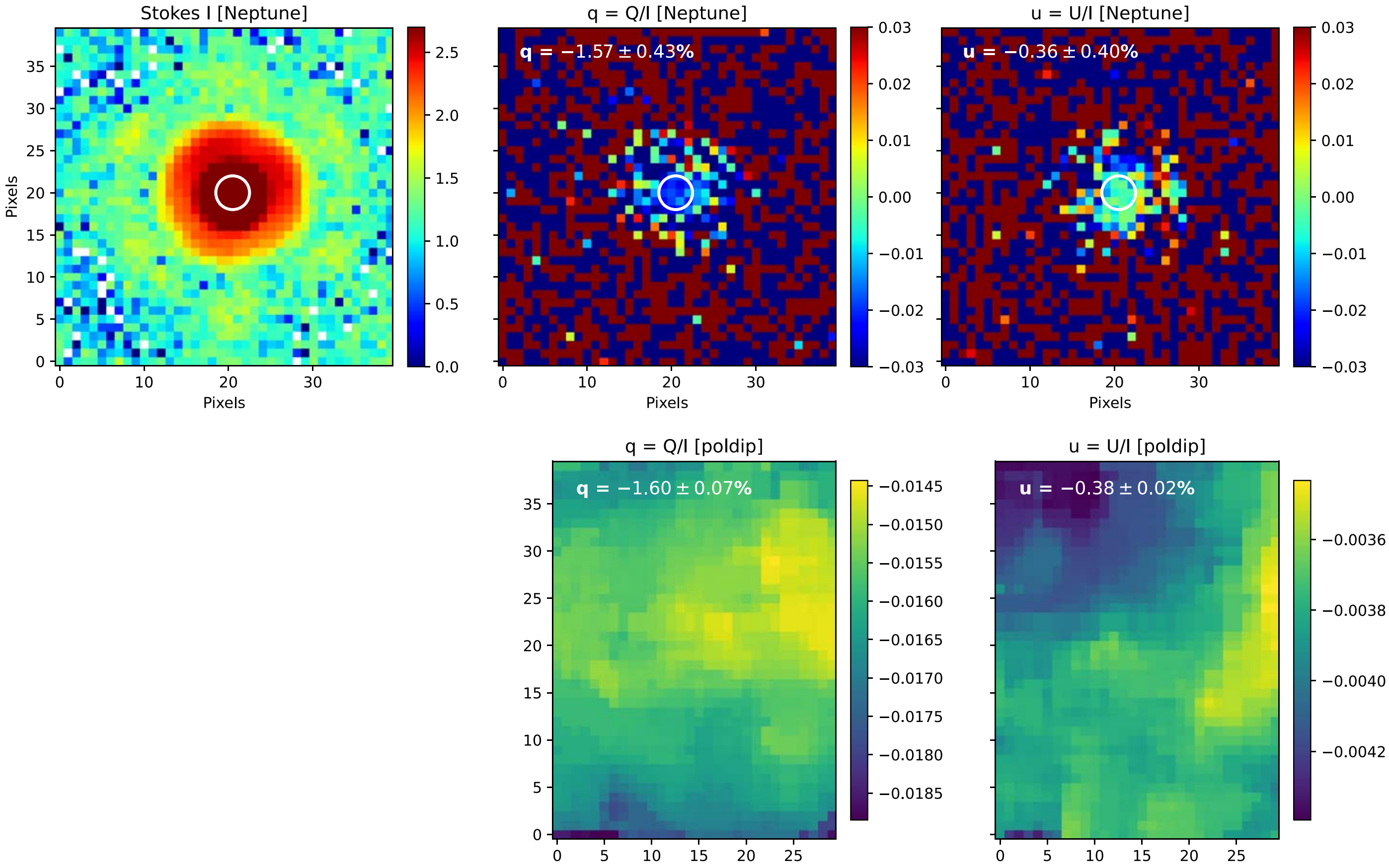

Figure 14. OTFMAP polarimetric observations of a planet (Neptune) and polarization skydip (poldip) at 53 μm. Top panels: polarization observations of a planet. Stokes I (left) in $\log_{10}$ scale, normalized Stokes $q = Q/I$ (middle), and $u = U/I$ (right) are shown. The FOV is 40 × 40 pixels (48 × 48 arcsec^2, with pixel scale of $1\overset{\prime\prime}{.}21$). Bottom panels: polarization observations of a skydip. Normalized Stokes $q = Q/I$ (middle) and U/I (right) are shown. The FOV is 32 × 40 pixels (82 × 102 arcsec^2, with a pixel scale of $2\overset{\prime\prime}{.}55$). Definitions and details of the estimation of the IP are described in Sections 2.5 and 3.3.

Appendix C
OTFMAP versus C2N for Circinus

OTFMAP and C2N comparisons for the observations of Circinus at 89 μm. Figure 15 shows the instrumental configuration and polarization maps for both observing modes. Figure 16 presents the histograms of the total and polarized flux and their standard deviations. The 1:1 plots of the polarization fraction and polarization angle are shown.

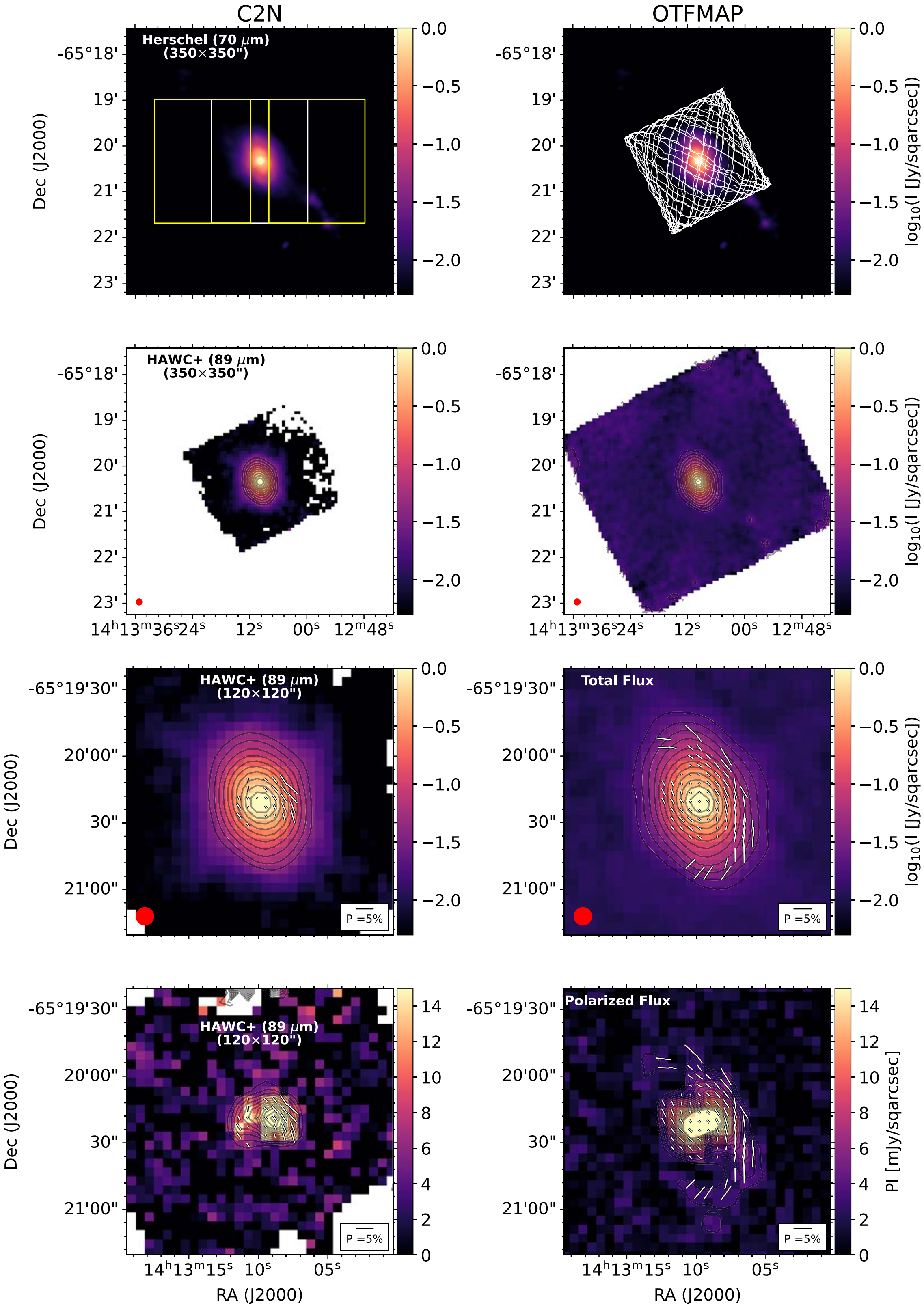

Figure 15. Comparison between C2N (left) and OTFMAP (right) observations of Circinus at 89 μm. First row: Herschel observations at 70 μm (color scale) of Circinus within an FOV of 350 × 350 arcsec^2 with overlaid C2N (left) and OTFMAP (right) configurations. For C2N, on-source (white) and off-source (yellow) positions with the FOV of HAWC+ at 89 μm are shown. For OTFMAP, the Lissajous curve (white solid line) of the scan is shown. Second row: HAWC+ total flux observations for C2N and OTFMAP within the same FOV as above. Contours start at $32\sigma_I$ and increase in steps of $2^n\sigma$, where $n = 5, 5.5, 6, \ldots$ and $\sigma_I = 0.3$ mJy arcsec^{-2}. The beam size is shown as a red circle in the bottom left. Third row: same as above within an FOV of 120 × 120 arcsec^2. Polarization measurements (white lines) are shown for $P/\sigma_P \geqslant 3$, $\mathrm{PI}/\sigma_{\mathrm{PI}} \geqslant 3$, $P < 30\%$, and $I/\sigma_I \geqslant 50$. A 5% polarization measurement is shown at the bottom right. Fourth row: HAWC+ polarized flux observations (color scale) within the same FOV and polarization as above. Contours start at $3\sigma_{\mathrm{PI}}$ and increase in steps of $1\sigma_{\mathrm{PI}}$, where $\sigma_{\mathrm{PI}} = 0.45$ mJy arcsec^{-2}.

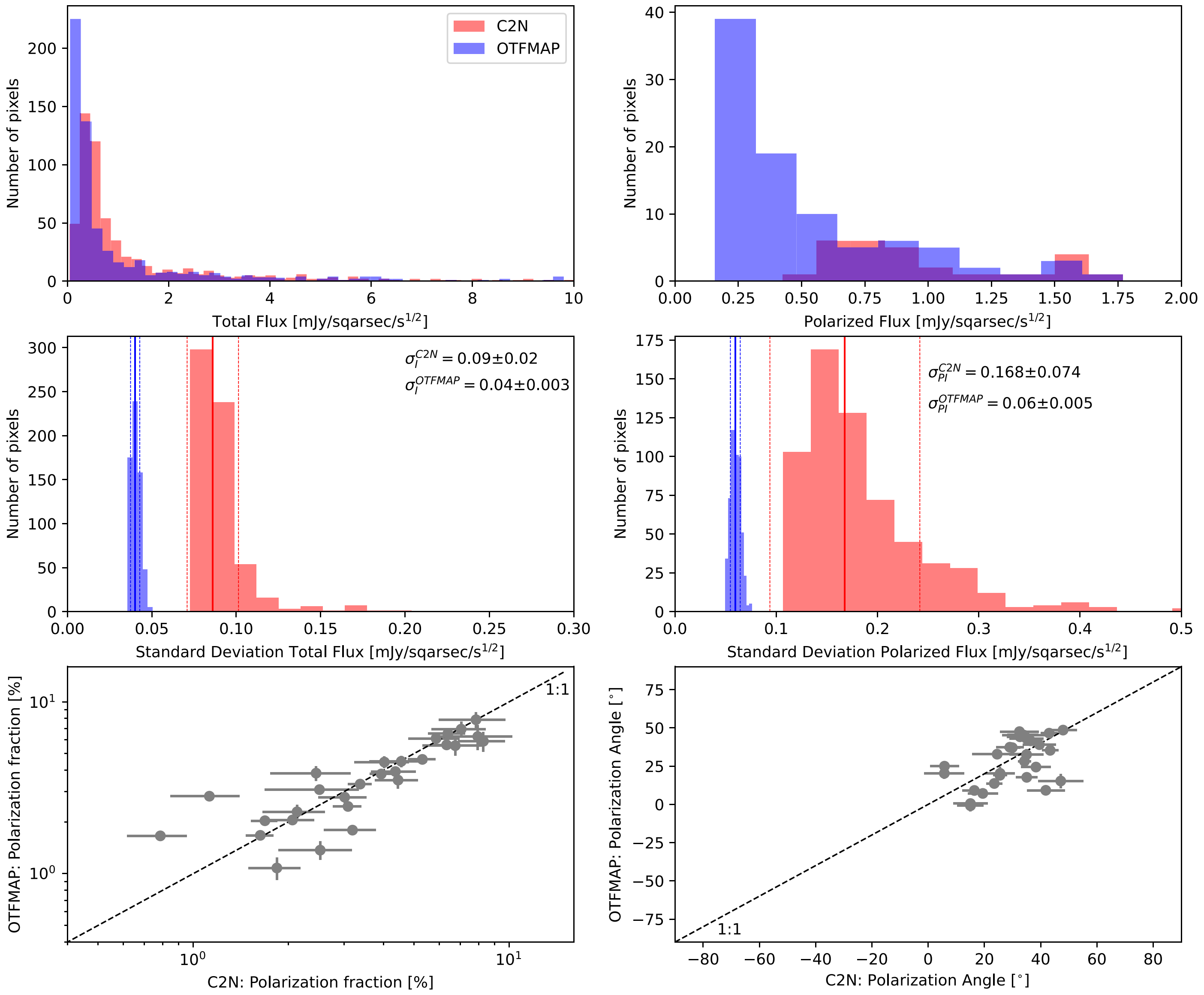

Figure 16. Sensitivity comparison between C2N (red) and OTFMAP (blue) observations of Circinus at 89 μm. Histograms of the total intensity (top left), polarized intensity (top right), standard deviations of the total flux (middle left), and polarized flux (middle right) are shown. The median and 1σ uncertainty of the distribution of the standard deviations are shown in the middle panels. The polarization fraction (bottom left) and polarization angle (bottom right) for C2N and OTFMAP observations are shown. A 1:1 line (black dashed line) is shown.

ORCID iDs

Enrique Lopez-Rodriguez https://orcid.org/0000-0001-5357-6538
William Vacca https://orcid.org/0000-0002-9123-0068
Simon Coude https://orcid.org/0000-0002-0859-0805
John E. Beckman https://orcid.org/0000-0001-5747-7086
Alejandro S. Borlaff https://orcid.org/0000-0003-3249-4431
Susan E. Clark https://orcid.org/0000-0002-7633-3376
Daniel A. Dale https://orcid.org/0000-0002-5782-9093
Sergio Martin-Alvarez https://orcid.org/0000-0002-4059-9850
Evangelia Ntormousi https://orcid.org/0000-0002-4324-0034
William T. Reach https://orcid.org/0000-0001-8362-4094
Julia Roman-Duval https://orcid.org/0000-0001-6326-7069
Konstantinos Tassis https://orcid.org/0000-0002-8831-2038

References

Astropy Collaboration, Robitaille, T. P., Tollerud, E., et al. 2013, A&A, 558, A33
Borlaff, A. S., Lopez-Rodriguez, E., Beck, R., et al. 2021, ApJ, 921, 128
Burtscher, L., Politopoulos, I., Fernández-Acosta, S., et al. 2020, Proc. SPIE, 11447, 114477L
Cantalupo, C. M., Borrill, J. D., Jaffe, A. H., Kisner, T. S., & Stompor, R. 2010, ApJS, 187, 212
Chapin, E. L., Berry, D. S., Gibb, A. G., et al. 2013, MNRAS, 430, 2545
Do well, C. D., Cook, B. T., Harper, D. A., et al. 2010, Proc. SPIE, 7735, 77356H
Emerson, D. T., & Graeve, R. 1988, A&A, 190, 353
Gordon, M. S., Lopez-Rodriguez, E., Andersson, B. G., et al. 2018, arXiv:1811.03100
Harper, D. A., Runyan, M. C., Dowell, C. D., et al. 2018, JAI, 7, 1840008
Haslam, C. G. T. 1974, A&AS, 15, 333
Hildebrand, R. H., Davidson, J. A., Dotson, J. L., et al. 2000, PASP, 112, 1215
Hunter, J. D. 2007, CSE, 9, 3
Johnson, B. R., Collins, J., Abroe, M. E., et al. 2007, ApJ, 665, 42
Kovács, A. 2006, PhD thesis, Caltech

Kovács, A. 2008a, Proc. SPIE, 7020, 702007
Kovács, A. 2008b, Proc. SPIE, 7020, 70201S
Li, P. S., Lopez-Rodriguez, E., Ajeddig, H., et al. 2022a, MNRAS, 510, 6085
Li, P. S., Lopez-Rodriguez, E., Soam, A., & Klein, R. I. 2022b, MNRAS, 514, 3024
Lopez-Rodriguez, E. 2021, NatAs, 5, 604
Lopez-Rodriguez, E., Beck, R., Clark, S. E., et al. 2021, ApJ, 923, 150
Lopez-Rodriguez, E., Dowell, C. D., Jones, T. J., et al. 2020, ApJ, 888, 66
Lopez-Rodriguez, E., Mao, S. A., Beck, R., et al. 2022, arXiv:2205.01105
Müller, P., Krause, M., Beck, R., & Schmidt, P. 2017, A&A, 606, A41
Ohsawa, R., Sako, S., Miyata, T., et al. 2018, ApJ, 857, 37
Patanchon, G., Ade, P. A. R., Bock, J. J., et al. 2008, ApJ, 681, 708
Reichertz, L. A., Weferling, B., Esch, W., & Kreysa, E. 2001, A&A, 379, 735
Robitaille, T., & Bressert, E. 2012, APLpy: Astronomical Plotting Library in Python, ascl:1208.017
Roussel, H. 2013, PASP, 125, 1126
Siringo, G., Kovács, A., Kreysa, E., et al. 2012, Proc. SPIE, 8452, 845206
Siringo, G., Kreysa, E., Kovács, A., Menten, K. M., & Forbrich, J. 2010, Proc. SPIE, 7741, 774108
Tegmark, M. 1997, PhRvD, 56, 4514
Vaillancourt, J. E., Chuss, D. T., Crutcher, R. M., et al. 2007, Proc. SPIE, 6678, 66780D
Ward-Thompson, D., Pattle, K., Bastien, P., et al. 2017, ApJ, 842, 66
Waskett, T. J., Sibthorpe, B., Griffin, M. J., & Chanial, P. F. 2007, MNRAS, 381, 1583
Weferling, B., Reichertz, L. A., Schmid-Burgk, J., & Kreysa, E. 2002, A&A, 383, 1088